

University of Mississippi

eGrove

---

Electronic Theses and Dissertations

Graduate School

---

2013

## Nanoenhanced Polyurea As A Blast Resistant Coating For Concrete Masonry Walls

Heather Kathryn Daniell Rivera  
*University of Mississippi*

Follow this and additional works at: <https://egrove.olemiss.edu/etd>



Part of the [Civil Engineering Commons](#)

---

### Recommended Citation

Rivera, Heather Kathryn Daniell, "Nanoenhanced Polyurea As A Blast Resistant Coating For Concrete Masonry Walls" (2013). *Electronic Theses and Dissertations*. 427.  
<https://egrove.olemiss.edu/etd/427>

This Dissertation is brought to you for free and open access by the Graduate School at eGrove. It has been accepted for inclusion in Electronic Theses and Dissertations by an authorized administrator of eGrove. For more information, please contact [egrove@olemiss.edu](mailto:egrove@olemiss.edu).

NANOENHANCED POLYUREA AS A BLAST RESISTANT COATING FOR CONCRETE  
MASONRY WALLS

A Thesis

presented in partial fulfillment of requirements  
for the degree of Master of Science in Engineering Science  
in the Department of Civil Engineering  
The University of Mississippi

by

Heather Kathryn Daniell Rivera

May 2013

Copy Right Heather K. D. Rivera 2013

ALL RIGHTS RESERVED

## ABSTRACT

Blast impact is a major concern in the world today. The leading cause of death due to blast impacts is rapidly moving debris. To prevent this many researchers are looking for methods of improved blast resistance for concrete masonry walls. However, many available protective coatings are not flame retardant. This thesis focuses on nanoenhanced polyurea for applications in improving blast resistance, while possessing improved flame retardancy, of concrete masonry walls. The polyurea that is being researched is enhanced with nanoadditives in an effort improve both blast and fire resistance. These materials are dynamically tested and those showing marked improvement are chosen for experimental and computational testing.

## ACKNOWLEDGEMENTS

I would like to express my appreciation to my advisor, Dr. Ahmed Al-Ostaz, and my co-advisor, Dr. Hunain Alkhateb, as well as my committee member, Dr. Alex Cheng. I would like to acknowledge the funding received under a subcontract from the Department of Homeland Security- sponsored Southeast Region Research Initiative (SERRI) at the Department of Energy's Oak Ridge National Laboratory that made this research possible.

I would also, like to thank Dr. Xiaobing Li for providing and developing the specimens used in this research.

Additionally, I would like to thank my fellow research assistants in the Nano-Infrastructure Research Group for their assistance and support over the last two years.

## TABLE OF CONTENTS

ABSTRACT.....	ii
ACKNOWLEDGEMENTS.....	iii
LIST OF TABLES.....	vi
LIST OF FIGURES .....	viii
I. INTRODUCTION.....	1
1.1 Literature Review.....	1
1.1.1 Techniques for Improved Blast Resistant Structures.....	1
1.1.2 Dynamic Mechanical Analysis .....	2
1.1.3 Multifunctional Materials .....	4
1.1.4 Experimental Setup.....	5
1.1.5 Computational Modeling .....	6
1.2 Background .....	7
1.2.1 Phase I.....	7
1.2.2 Phase II.....	8
1.3 Motivation .....	9
1.4 Objectives.....	10
II. SUMMARY OF MATERIALS USED .....	12
2.1 Polyurea (PU) .....	12
2.2 Nano-Additives.....	12
III. DYNAMIC MECHANICAL ANALYSIS.....	15
IV. MATERIAL MULTIFUNCTIONALITY.....	31
4.1 Multi-functionality for Blast and Fire Loading .....	31
4.2 Multi-functionality Index of NPRC.....	36
V. DETAILED EVALUATION OF MATERIALS .....	38
5.1 Experimental Setup .....	38

5.2	Experimental Analysis .....	41
5.3	Experimental Test Results.....	43
5.3.1	Test 1 Results .....	44
5.3.2	Test 2 Results .....	45
5.3.3	Test 3 Results .....	45
5.3.4	Test 4 Results .....	46
5.3.5	Test 5 Results .....	46
5.3.6	Test 6 Results .....	47
5.3.7	Test 7 Results .....	47
5.3.8	Test 8 Results .....	48
5.4	Computational Modeling of CMU Panels Subjected to Air Blast Loading Using Finite Element Method.....	48
5.4.1	Finite element configuration and mesh.....	49
5.4.2	Material Models and Parameters .....	50
5.5	Numerical Simulation of Experiment Results.....	54
5.5.1	Wall #1 Results .....	54
5.5.2	Wall #2 Results .....	55
5.5.3	Wall #3 Results .....	56
5.5.4	Wall #4 Results .....	57
5.5.5	Wall #5 Results .....	58
5.6	Parametric Evaluation .....	61
5.6.1	Adhesion .....	61
5.6.2	Full Scale Validation.....	70
5.6.3	Thickness Evaluation .....	73
5.6.4	Single Degree of Freedom .....	76
VI.	CONCLUSION .....	83
	REFERENCES .....	87
	APPENDIX.....	90
	VITA.....	113

## LIST OF TABLES

Table 1: List of nanocomposites with best DMA properties in each class .....	25
Table 2: Polyurea Nano-Composites Layers Coated on ¼ scale blocks for Fire Test.....	32
Table 3: Polyurea Sheet Materials .....	39
Table 4: Test Specimen Description .....	39
Table 5: Summary of Test Results.....	44
Table 6: Material Models.....	52
Table 7: Mechanical Properties of PUNO .....	52
Table 8: Stress-Strain Values for PUNO .....	52
Table 9: Mechanical Properties of PUPM3PO .....	53
Table 10: Stress-Strain Values of PUPM3PO .....	53
Table 11: Mechanical Properties of EG10APP10PO .....	53
Table 12: Stress-Strain Values for EG10APP10PO .....	54
Table 13: Deformation and failure shapes obtained numerically and experimentally for the case of CMU wall retrofitted with single layer PUNO (Wall #1) .....	55
Table 14: Deformation and failure shapes obtained numerically and experimentally for the case of CMU wall retrofitted with single layer PUNO (Wall #2) .....	56
Table 15: Deformation and failure shapes obtained numerically and experimentally for the case of CMU wall retrofitted with double layer PUPM3PO +EG10APP10PO (Wall #3).....	57



Table 16: Deformation and failure shapes obtained numerically and experimentally for the case of CMU wall retrofitted with single layer PUPM3PO (Wall #4) .....	58
Table 17: Deformation and failure shapes obtained numerically and experimentally for the case of CMU wall retrofitted with double layer PUPM3PO +EG10APP10PO (Wall #5).....	59
Table 18: Midpoint deflection .....	60
Table 19: Maximum Midpoint Deflection between Models for Wall#1 .....	61
Table 20: Maximum Midpoint Deflection between Models for Wall#2 .....	62
Table 21: Maximum Midpoint Deflection between Models for Wall#3 .....	63
Table 22: Maximum Midpoint Deflection between Models for Wall#4 .....	64
Table 23: Maximum Midpoint Deflection between Models for Wall#5 .....	65
Table 24: Maximum Midpoint Deflection between Models for Wall#6 .....	66
Table 25: Maximum Midpoint Deflection between Models for Wall#7 .....	67
Table 26: Midpoint Deflection Comparison of Bonding.....	69
Table 27: Stress-Inertia Scaling (Irshidat et al. 2011) .....	71
Table 28: 1/4 <sup>th</sup> scale vs. Full scale for PUNO Coating.....	71
Table 29: 1/4 <sup>th</sup> scale vs. Full scale for PUPM3PO+EG10APP10PO Coating.....	72
Table 30: 1/4 <sup>th</sup> scale vs. Full scale for PUPM3PO Coating.....	73
Table 31: Transformation Factors (Biggs 1964).....	77

## LIST OF FIGURES

Figure 1: Q800 Dynamic Mechanical Analyzer .....	16
Figure 2: DMA Tension Film Clamp (Thermal Analysis 2010) .....	16
Figure 3: Effect of Frequency on Mechanical Properties in Polymers (Oliver et al. 2004) .....	17
Figure 4: DMA Frequency Sweep Test Results for PUNO and Calcium Sulfate Nanocomposites .....	18
Figure 5: DMA Frequency Sweep Test Results for PUNO and Fly Ash Nanocomposites.....	18
Figure 6: DMA Frequency Sweep Test Results for PUNO and Nanoclay Nanocomposites .....	19
Figure 7: DMA Frequency Sweep Test Results for PUNO and PM POSS Nanocomposites .....	19
Figure 8: DMA Frequency Sweep Test Results for PUNO and (PM+AM) POSS Nanocomposites .....	20
Figure 9: DMA Frequency Sweep Test Results for PUNO and Expandable Graphene + Ammonium Polyphosphate Nanocomposites.....	20
Figure 10: Low strains tensile response of PUNO and CS nanocomposites .....	22
Figure 11: Low strains tensile response of PUNO and FA nanocomposites .....	22
Figure 12: Low strains tensile response of PUNO and NC nanocomposites .....	23
Figure 13: Low strains tensile response of PUNO and PM POSS nanocomposites.....	23
Figure 14: Low strains tensile response of PUNO and (PM+AM) POSS nanocomposites .....	24
Figure 15: Low strains tensile response of PUNO and EG + Ammonium polyphosphate nanocomposites.....	24
Figure 16: Summary of DMA testing results for Polyurea nanocomposites .....	25
Figure 17: Tan $\delta$ variation during DMA testing for PUNO and calcium sulfate nanocomposites	26

Figure 18: Tan $\delta$ variation during DMA testing for PUNO and fly ash nanocomposites .....	27
Figure 19: Tan $\delta$ variation during DMA testing for PUNO and nanoclay nanocomposites.....	27
Figure 20: Tan $\delta$ variation during DMA testing for PUNO and PM-POSS nanocomposites .....	28
Figure 21: Tan $\delta$ variation during DMA testing for PUNO and (PM+AM) POSS nanocomposites .....	28
Figure 22: Tan $\delta$ variation during DMA testing for PUNO and Expandable graphite + Ammonium polyphosphate nanocomposites .....	29
Figure 23: Multi-functionality Performance of Selected Nano-composites .....	34
Figure 24: Validation of Multi-functionality performance of selected nanocomposites using blast and fire tests. ....	35
Figure 25: Multi-functionality for Various Nano-enhanced Polymeric Materials .....	37
Figure 26: Test Specimen with Applied Polyurea Sheet .....	40
Figure 27: Bottom Tube Clamping Polyurea Sheet .....	40
Figure 28: Estimated P-I Diagrams for Test Specimen 1 .....	43
Figure 29: a) Wall geometry (b) F.E. Mesh.....	50
Figure 30: Midpoint deflection represented in a bar chart for the experimental vs. simulation (no bonding, bonding).....	69
Figure 31: Full Scale Wall: (a) Geometry (b) F. E. Mesh .....	70
Figure 32: P-I Curve for PUNO.....	74
Figure 33: P-I Curve for PUPM3PO+EG10APP10PO.....	75
Figure 34: P-I Curve for PUPM3PO.....	75
Figure 35: Triangular Load Approximation (Irshidat 2010).....	76
Figure 36: Stress-Strain Curve for a commercial Polyurea (Irshidat 2010) .....	78

Figure 37: Resistance Function for a Pure Polyurea (Irshidat 2010).....	79
Figure 38: Stress-Strain Curve for PUNO .....	80
Figure 39: Resistance Function for PUNO .....	80
Figure 40: Stress-Strain Curve for PUPM3PO .....	81
Figure 41: Stress-Strain Curve for EG10APP10PO .....	81
Figure 42: Resistance Function for PUPM3PO .....	82
Figure 43: Resistance Function for PUPM3PO+EG10APP10PO .....	82

## I. INTRODUCTION

The improvement of blast resistance in structures is a topic of great interest in today's world. The leading cause of death from blast load impact is typically not related to the actual blast effects such as heat or pressure, it is the debris and fragmentation moving at exceedingly high velocities (Raman et al. 2011). Over the last decade there have been many developments in means of improving blast resistance. These developments mainly include adding a type of retrofit material to the structure through spray or adhesion. These materials include specimens like fiber reinforced polymers, glass fiber reinforced polymers, polyurea, polyurethane, etc. (Raman et al. 2011).

### 1.1 Literature Review

#### 1.1.1 Techniques for Improved Blast Resistant Structures

There are various techniques that have been studied and developed as a means of improving the blast resistance of a structure. One method of improvement is to increase the mass by the addition of concrete or steel to the structure (Raman et al. 2011). However, this is determined to be unsafe because it increases the dead load in the structure and the gravity load in its bearing elements (Razaqpur et al. 2009). Since the addition of concrete and steel is both expensive and not as effective other alternatives have been considered. The majority of alternatives revolve around the addition of a composite or polymer retrofit material (Davidson et al. 2005). Among the most common laminates being considered for the blast resistance include fiber-

reinforced polymers (FRP). These are utilized for several reasons including: they possess a high strength to weight ratio, they are typically corrosion free, and cost effective. Raman et. al. primarily focused on carbon FRP and glass FRP (Raman et al. 2011). However, both carbon and glass FRPs are limited because they require a large quantity of layers to perform properly, and during close-in detonations the strain demand exceeds the strain capacity which potentially leads to premature debonding or delamination of the reinforcement with the Concrete Masonry Unit (CMU) wall (Raman et al. 2011).

Davidson et al. (2005) utilized thirteen spray-on polymers as a means of improving blast resistance. These polymers included polyurethanes, a polyurea, and several that are a combination of both polyurethane/polyurea. These are selected because they possessed fast gel and cure time which made them feasible for application to a vertical structure. Furthermore, it is determined that pure polyurea possessed better stiffness and elongation capacity which made it the prime candidate for blast testing. The spray-on technique allowed for it to form a stronger bond with CMU wall. It is concluded that a strong bond is necessary for the polymer coating to be considered effective. Spray-on polymers are deemed both costs effective and adequately deterred fragmentation during blast loading (Davidson et al. 2005).

### **1.1.2 Dynamic Mechanical Analysis**

Dynamic mechanical analysis testing of polymer materials is performed to obtain the mechanical properties of the specimen. There are several ways that are commonly utilized to perform testing. The method chosen is dependent upon the mechanical properties needed for the individual study.

Yi et al. (2005) utilized dynamic mechanical analysis to perform temperature sweeps to determine the phase transition temperature of polyurea and polyurethanes. These temperature sweeps are initially performed at constant frequency of 1Hz and a constant strain rate 0.1%. Then, the temperature is varied from -156°C to 80°C with a temperature ramp of 3°C/min. Each temperature sweep is repeated for 10 Hz and 100 Hz and equivalent strain rates. By performing this test at various frequencies any shifts in the phase transition can be determined in relation to its strain rate dependence. These tests found that polyurea makes a transition to a rubbery phase at lower strain rates, and a glassy phase at higher strain rates (Yi et al. 2005).

MacAloney et al. (2007) utilized dynamic mechanical analysis to characterize viscoelastic properties of aliphatic polyurethane interlayers in the frequency domain through the linear viscoelastic theory. For this characterization frequency sweeps are performed. Generally, frequency sweeps are performed at constant temperature and amplitude. During this process the material's response to the frequency is recorded (Dynamic Mechanical Analysis (DMA) 2006). This paper performs multi-frequency sweeps in which the temperature increases in steps and the machine equilibrates for 5 minutes at that temperature then a frequency sweep is run at that from 0.1 Hz to 100 Hz at that temperature. This process is repeated from -100°C to 50°C in increments of 3°C. The process determines rate-dependent behavior of the material (MacAloney et al. 2007).

The nanoenhanced composites that are being used in the work presented are viscoelastic materials. The properties of these materials are greatly impacted by

their loading frequencies. These being the case frequency sweeps are selected as the dynamic mechanical analysis testing for the given materials in this research.

### **1.1.3 Multifunctional Materials**

Multifunctional materials are materials that are uniquely designed to meet a specific set of requirements. Salonitis et al. (2009) suggests that glass or carbon fiber reinforced plastics is an example of multifunctional structural composite material. This material is considered as such because of its ability to have its strength and stiffness properties engineered through the material selection to meet predefined demands.

Another advance in the structural composite materials is the ability to self-healing. Kessler et al. presents (2003) presents a fiber-reinforced polymer matrix composite material that has a self-healing ability. For this material a healing agent, microcapsule shell, and chemical catalyst are added to the matrix to improve its healing ability. Once a microfracture occurs the healing agent becomes active which triggers the catalyst which then polymerizes and bonds the microcrack together. This multifunctional ability allows the structure to resume 45% of the pre-fracture toughness at room temperature (Kessler et al. 2003).

Multifunctional composites are of growing importance in terms of blast resistance. Ibeh et al. (2007) states that a hybrid of high strength materials, like ceramics and high strength metals, and high strength/stiffness materials, like viscoelastic polymeric fibers, are necessary to effectively resist blast impact. The combination of the two may provide a damping effect on the impact energy



absorption and increase stiffness, strength, and flame retardancy. Many polymeric composites today are being researched to meet these demands as discussed in the Techniques for Improved Blast Resistant Structures section.

#### **1.1.4 Experimental Setup**

Multiple set ups are employed in different studies in order to experimentally test the capabilities of the retrofit materials on CMU walls when subject to blast loading. The majority of the research does agree that the CMU wall should be simply supported on the top and fixed on the bottom, there are differing methods for how to achieve this support system. Also, the existing research varies on the chosen method for experimental blast loading.

Davidson et al. (2005) constructed full scale CMU walls using standard construction materials and practice for an unreinforced concrete infill masonry. For this wall mortar is applied in 9.5 mm thickness on the front and back faces, however it is not used on the webs. The CMU walls are stabilized inside a reaction structure which is created for the withstanding of blast loading. The top and bottom are laterally restrained, translation on the vertical edges permits one-way flexural response. To create the blast loading for this CMU wall explosive charges are detonated at pre-designed stand-off distances (Davidson et al. 2005).

Maji et al. (2008) an alternative set up is used in which a room is constructed with four CMU walls that are 6.1 m x 3.7 m and 4 m in height. These are tied together at their corners with interlacing CMU blocks. These walls are reinforced horizontally at every third course. The testing walls are built inside a

reaction structure similar to the one used by Davidson et al. (2005). The beams in the system and the floor create the simple supports. For this research a spherical blast is created by placing a charge in the room's center at a height of 0.76 m (Maji et al. 2008).

Oesterle et al. (2009) developed another experimental test setup. The top of the CMU wall is simply supported through a bearing reaction with a concrete slab that is supported by a movable reaction block. This setup allowed the top to vertically rotate and translate during loading. The base of the CMU wall is fixed supported as it is connected to a reinforced concrete footing. To generate a blast load this research uses a blast load generator which is a system of extremely rapid nitrogen/hydraulic oil driven actuators. This allows the researchers to control and quickly repeat impact loadings for the simulation of blast loading conditions. The advantage of a blast generator is that it does not use actual explosives during testing (Oesterle et al. 2009).

### **1.1.5 Computational Modeling**

Computational modeling of blast loadings is one of the most cost effective and safe ways to determine the ability of a retrofit material to improve blast resistance. Commonly finite element softwares are used for this modeling. The research shows that LS-DYNA or LS-DYNA 3D is used in various project to model blast loading experiments. A piecewise Drucker-Prager strength criterion is typically used to model the brick and mortar material (Wei et al. 2010). The polymer retrofit materials have to be individually input into the program; one

project used a piecewise linear plasticity model to input the retrofit material properties (Davidson et al. 2005). In all cases it seems that perfect bonding with the CMU wall is assumed for the model. To simulate the blast loading LS-DYNA calculates the load based on “ConWep” in which the stand-off distance, the free air burst, surface burst, and charge weight are defined (Wei et al. 2010).

## **1.2 Background**

### **1.2.1 Phase I**

The first phase of this research focused on the development and testing of nanoenhanced composites for blast resistant coatings. Irshidat et al (2011) explored the possibilities of utilizing nanoparticle reinforced polymeric materials as opposed to the commonly used fiber-reinforced polymeric materials. Polyurea is used as the polymeric materials and graphene nano platelets (XGnP), and polyhedral oligomeric silsesquioxane (POSS) are utilized as nanoparticle enhancers. The materials that are developed are tested using uni-axial direct tensile testing to determine which composites possess the most improved properties for experimental testing.

Then, experimental testing is performed at the U.S. Army Corp of Engineers Research and Development Center (ERDC) using quarter scale concrete masonry unit (CMU) walls that is 16 blocks in height and 12 blocks in width. The retrofit coating materials are applied using a spraying technique to the interior face of the CMU walls. Three walls are tested with approximately a 1.5 mm thick retrofit layer: one with polyurea alone, one with polyurea and XGnP and one with polyurea and POSS. The blast impact is simulated using air blast

cannon at a predefined impulse and pressure. The POSS material appears to significantly improve the performance of the polyurea whereas the XGnP does not. From these experiments a computational model is designed using ANSYS AUTODYN that can be used to predict the experiments (Irshidat 2011).

### **1.2.2 Phase II**

Phase I addresses the improved blast resistance of nanoenhanced polyurea coatings on concrete masonry walls. However, it does not address the secondary concern during a blast impact which is fire retardancy. Polymeric coatings while improving the blast resistance may, in some cases, increase the risk of a fire hazard.

Phase II evaluates the potential for a blast resistant coating to perpetuate the growth an existing fire caused by a blast impact. It investigated the following blast resistant materials: polyurea, polyurea with POSS and polyurea with exfoliated graphene platelets. Along with the blast resistant material four fire resistant materials are tested. First, testing is performed using a cone calorimeter heat release rate (HRR) measurements. Next, the flammability characterization and heat flux generated for the structural components and system are determined using the NIST Fire Dynamic Simulator (FDS), which exposes concrete columns and masonry walls to an existing fire. Full details on the phase II fire testing is given in the Appendix.

Based on the results it is seen that the blast resistant material coatings exhibit similar maximum heat flux and stress/strains. The polyurea with the

addition of XGnP and POSS results in a reduction in the HRR (Alkhateb et al. 2013).

### **1.3 Motivation**

The capacity to protect the United States' critical infrastructure is imperative to our national security, public safety, economic vitality, and way of life. Blast impact is a reality in today's world that threatens these things, as is evident from current events such as the explosions at the Boston Marathon 2013 where more than 100 people were reportedly injured from fragmentation and debris. Another incident was the explosion on the Deepwater Horizon oil rig in 2010 off the coast of Venice, LA. This explosion generated a massive fire that took approximately six firefighting vessels to put out. This explosion and the subsequent fire cost the lives of 11 oil rig workers and injured 16 others. A more deadly event was the infamous Oklahoma City bombing in 1995 in which a bomb was set off in the Alfred P. Murrah Federal Building. The blast debris, fragmentation, and ensuing fires damaged a 16 block radius including 324 buildings and claimed the lives of 168 people.

The improvement of structural endurance to both blast and fire resistance is vitally important as can be seen from current events. From the Literature Review and Background it is seen that much of the available research focuses on blast resistant coatings or fire retardant coatings for structures and their components. However, a material coating being either blast or fire resistant alone is not sufficient for adequate structural protection or safety precaution for inhabitants.

The motivation for this research is to design an optimal material that will perform as both blast and fire resistant coating. From the research acquired in Phase II, new nanoadditives with blast and fire resistant properties can be explored and utilized to create new composite materials. This research into improved material coatings is a key component in preserving our infrastructure and protecting the safety and well-being of our citizens.

#### **1.4 Objectives**

The objective of this work is to evaluate several nano modified composite materials through dynamic mechanical analysis to determine their mechanical properties and the improvement gained by the nanoenhancement. Then considerations are made for a multi-functionality analysis of the nanoenhanced composites in terms of their blast and fire resistance. After, these considerations the nanoenhanced composites are narrowed down based on their performance. Three nanocomposites systems were chosen for further experimental blast testing and computational simulations.

Objectives:

- 1) Select nanoenhanced composites that show marked improvement in dynamic and fire resistant properties.
- 2) Perform experimental testing on selected coating materials.
- 3) Apply the multi-functionality approach to optimize and select the best blast and fire performance nano-enhanced coatings.

- 4) Utilizing finite element simulations to validate the blast experiments and to predict the P-I curves.
- 5) Perform a parametric evaluation of the candidate materials.

## II. SUMMARY OF MATERIALS USED

This research utilized various materials for the enhancement of retrofit materials for improved blast resistance. These materials encompass one polymer and numerous nano-additives used for enhancement.

### **2.1 Polyurea (PU)**

Polyurea (PU) is the base polymer in this research. It is derived from a mixture of a diisocyanate component and a diamine component. There are two types of polyurea that have been utilized in this research. The first is a blast flex polyurea (BF), Tyfo Blast-Flex III. This polyurea is supplied by Fyfe Co. LLC, San Diego, CA, USA. The second type of polyurea is made from mixing Versa link P-1000 (VP1000) and Isonate 143L with a 4:1 ratio. These components are provided by Air Products and Chemical, Inc., Allentown, PA, USA and Dow Chemical Company, Midland, MI, USA, respectively.

### **2.2 Nano-Additives**

This research investigates two types of nano-additives. The first type of nano-additives, used for improved blast resistance and flame retardancy, includes: nano-clay, fly ash, Amine POSS, PM1285 POSS, and Calcium Sulfate. The second types of nano-additives are conventional flame retardant formulations,



used in the form of an applied coating, which includes additives like expandable graphene and Ammonium Polyphosphate.

### **2.2.1 Nano-Clay (NC)**

Nano-clay is a clay material that can be utilized as a protective layer on a flaming surface that helps prevent heat and mass transfer during a combustion reaction. The nano-clay is of Cloiste 30D and is provided by Southern Clay Products, Inc. Gonzales, TX, USA.

### **2.2.2 Fly Ash (FA)**

Fly Ash is a residue generated from a combustion reaction and can be utilized as a fire retardant. FA is also considered environmentally friendly and cost effective because it is a common industrial by-product. This material is provided by Boral Material Technology Inc., Corona, CA, USA.

### **2.2.3 Polyhedral Oligomeric Silsesquioxane (POSS)**

POSS is an organic/inorganic hybrid monomer, and is used as a possible solution for the improvement of mechanical properties in polymer nano-composites. There are two types of POSS that are used and added to a base PU; these include: Amine POSS (AM), AM0281, and PM1285 (PM) which is a fire retardant nano-additive. AM and PM are provided by Hybrid Plastics Inc., Hattiesburg, MS, USA.

### **2.2.4 Calcium Sulfate (CS)**

Calcium sulfate exists copiously in the natural environment, and is also found as an industrial byproduct. This product is purchased from Sigma-Aldrich Corp., St. Louis, MO, USA.

#### **2.2.5 Expandable Graphene (EG)**

Expandable graphene (EG) is a synthesized intercalation compound of graphite that is capable of expansion or exfoliation when heated. This being the case it is used as a fire retardant layer in this research. EG of type A3772 is provided by Asbury Carbons, Inc., Asbury, NJ, USA.

#### **2.2.6 Ammonium Polyphosphate (APP)**

Ammonium Polyphosphate swells when it is exposed to heat. This being the case it is commonly used as a fire retardant. Ammonium Polyphosphate of type Chek P/30 (regular) is supplied from ICL Performance Products Corp., St. Louis, MO, USA.

### III. DYNAMIC MECHANICAL ANALYSIS

Polyurea is a thermoplastic elastomer that is viscoelastic in nature. Due to its nature the temperature and loading rate impact its mechanical response. In dynamic mechanical analysis (DMA) testing, a small cyclic force is applied to the test specimen. The material response is recorded in terms of a storage modulus ( $E'$ ) and a loss modulus ( $E''$ ). The storage modulus is the measure of the elastic response of the material. The loss modulus characterizes the energy dissipation ability of the material. There is a phase lag between the applied load and the material response; this is called the tangent delta ( $\tan\delta$ ). The  $\tan\delta$  is calculated as the ratio of the loss modulus to the storage modulus.

DMA tests are performed for all nineteen nanocomposites materials using the Q800 series DMA, see Figure 1. Three specimens are tested for each nanocomposite, each with the dimensions of 6.3mm in width and approximately 25 mm in length. The frequency sweep test is performed on all material specimens using the tension clamp shown in Figure 2. The specimens are subjected to a loading that goes from 1-200 hertz at 50 hertz increments. The temperature and displacement are set as constants at 35°C and 15 $\mu$ m. The load is specifically chosen to allow the material behavior to remain in the elastic range. During the frequency sweep the viscoelastic response of the material is recorded in terms of its storage and/or loss modulus vs. the loading frequency.



**Figure 1: Q800 Dynamic Mechanical Analyzer**



**Figure 2: DMA Tension Film Clamp (Thermal Analysis 2010)**

In the mechanical testing of polymeric materials, the low loading frequencies are dominated by viscosity driven behavior. Also, as the loading frequency increases the

materials become stiffer and often exhibit elastic, solid-like behavior, as shown in Figure 3.

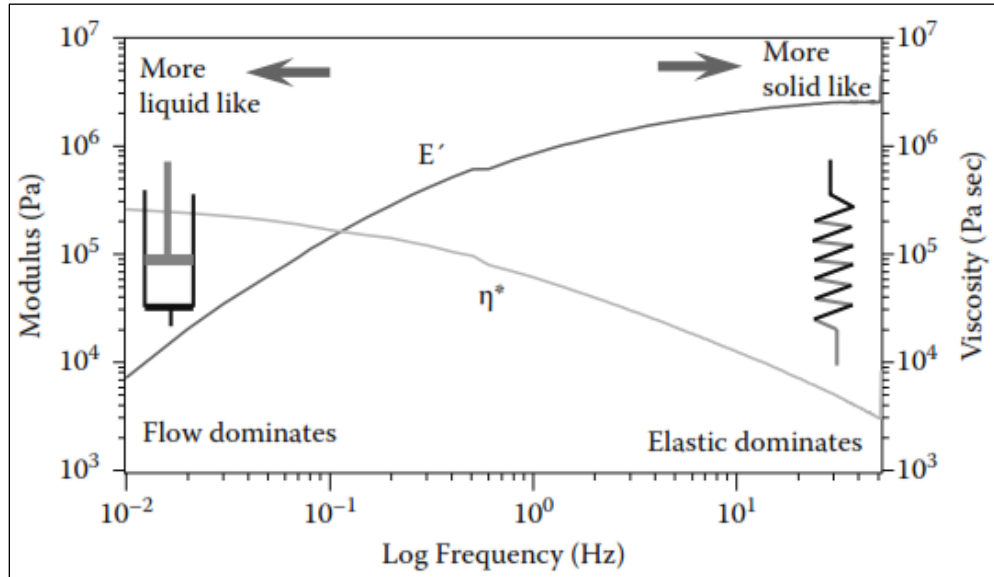


**Figure 3: Effect of Frequency on Mechanical Properties in Polymers (Oliver et al. 2004)**

The average storage modulus of PUNO with calcium sulfate, fly, nano clay, PM-POSS, various PM-POSS mixtures, and AM-POSS and various mixtures of expandable graphene and ammonium polyphosphate are provided in Figure 4, Figure 5, Figure 6, Figure 7, Figure 8, and Figure 9, respectively. In all figures the results of the pure PUNO control sample are plotted as a green reference line.

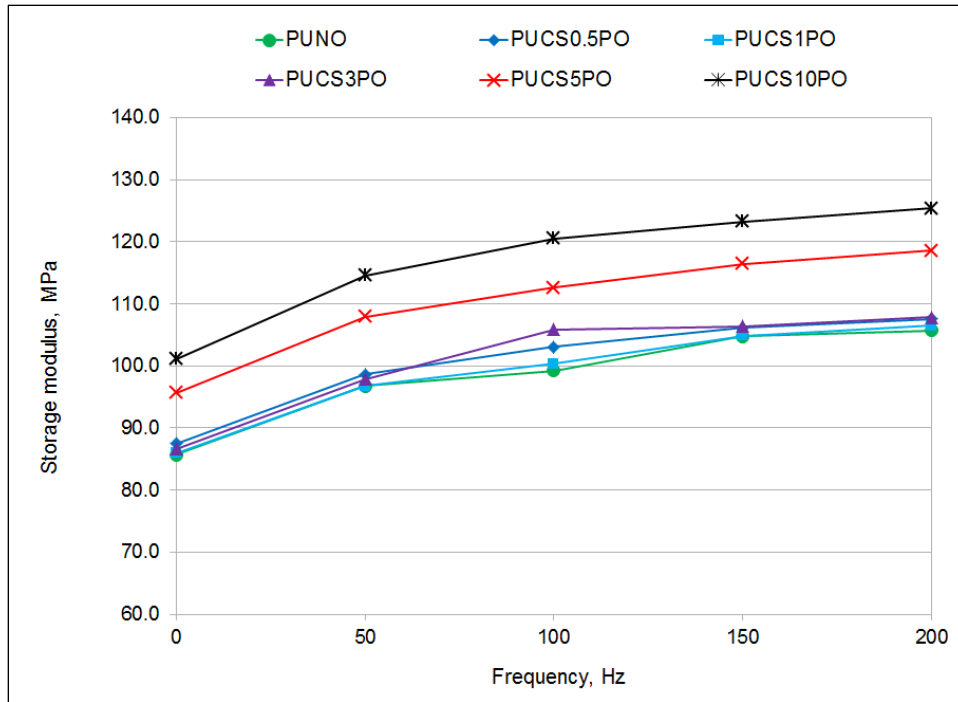


**Figure 4: DMA Frequency Sweep Test Results for PUNO and Calcium Sulfate Nanocomposites**

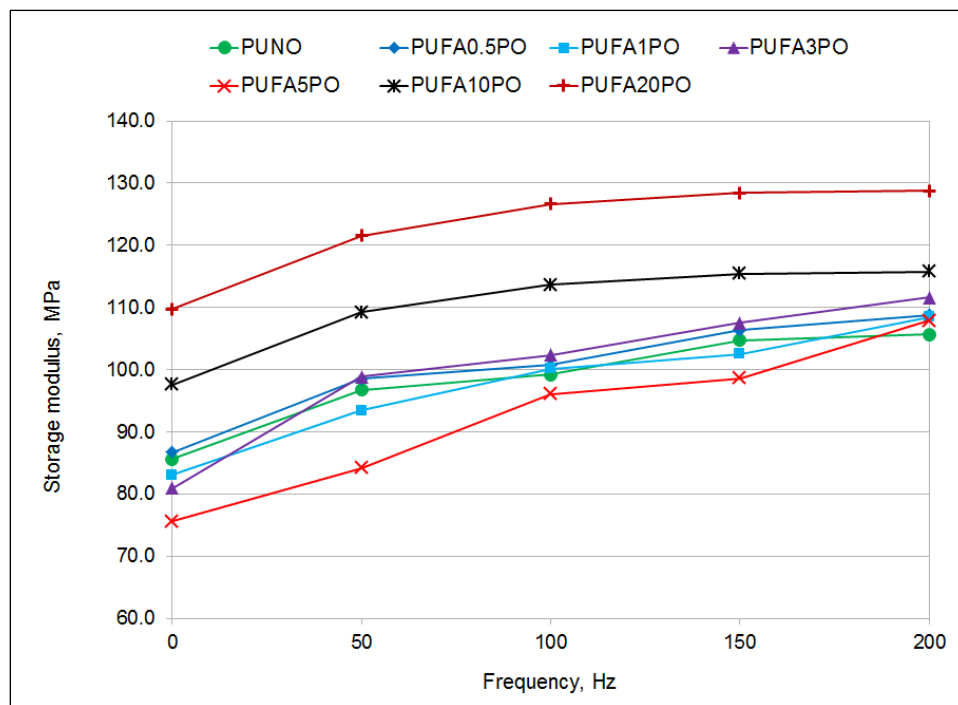


**Figure 5: DMA Frequency Sweep Test Results for PUNO and Fly Ash Nanocomposites**

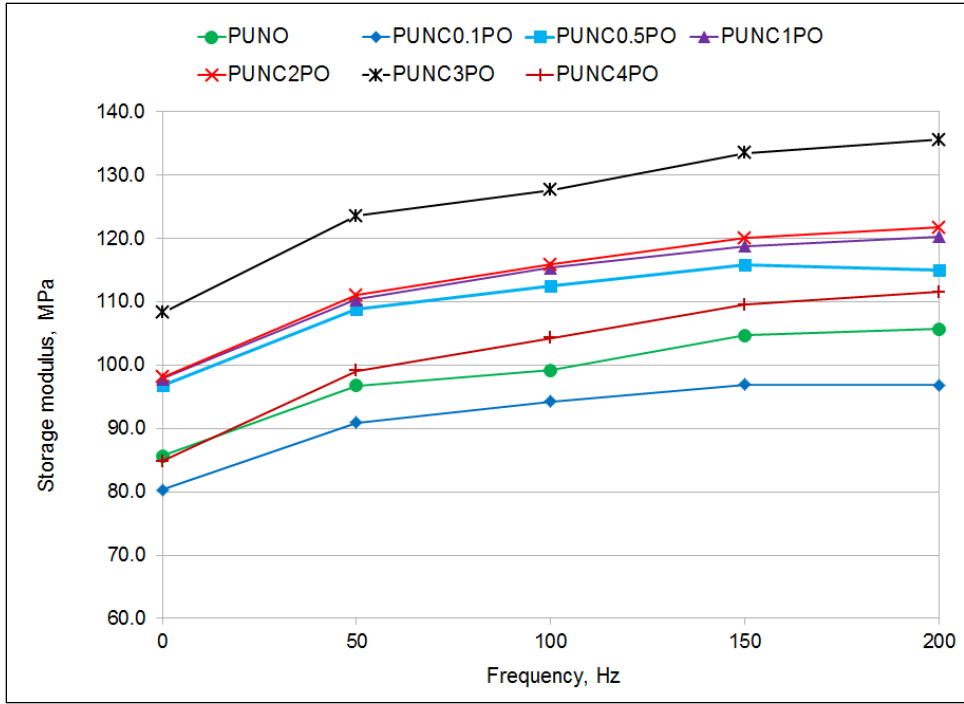


Figure 6: DMA Frequency Sweep Test Results for PUNO and Nanoclay Nanocomposites

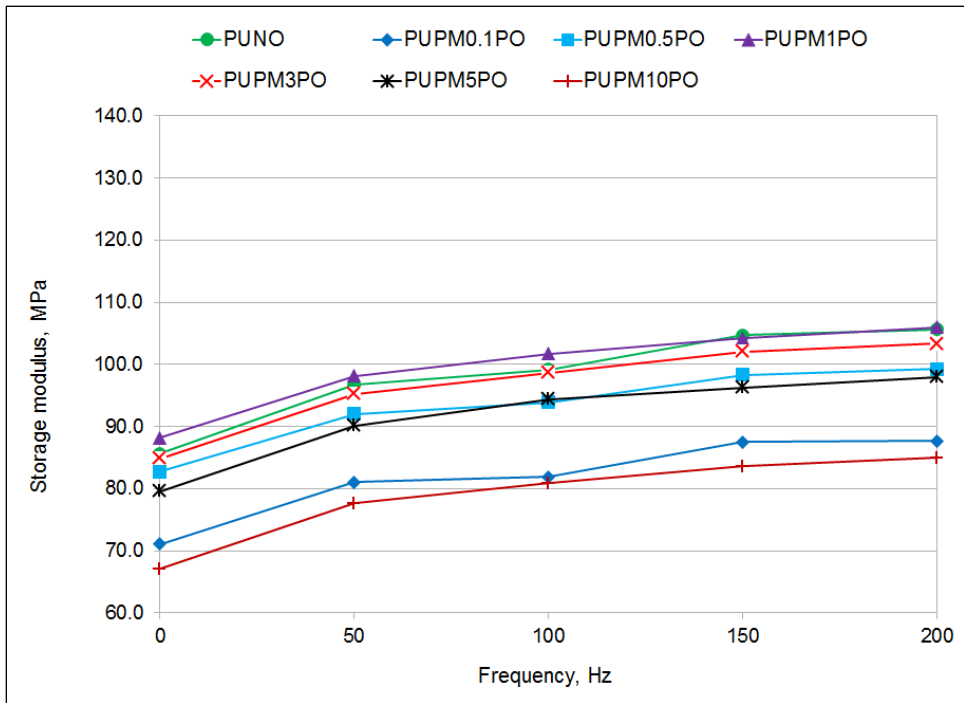
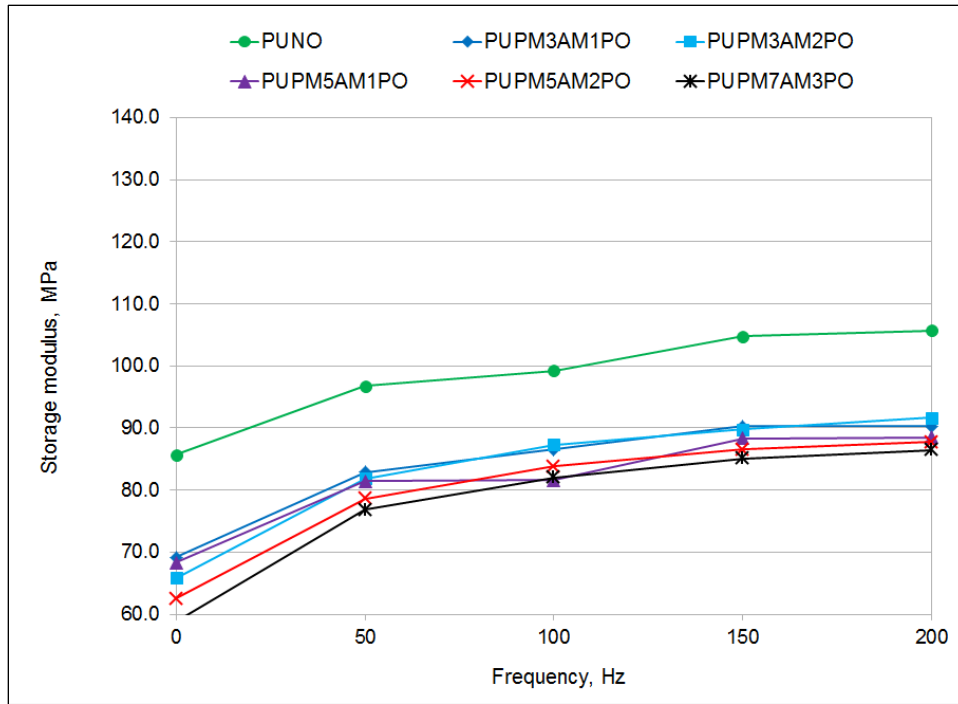
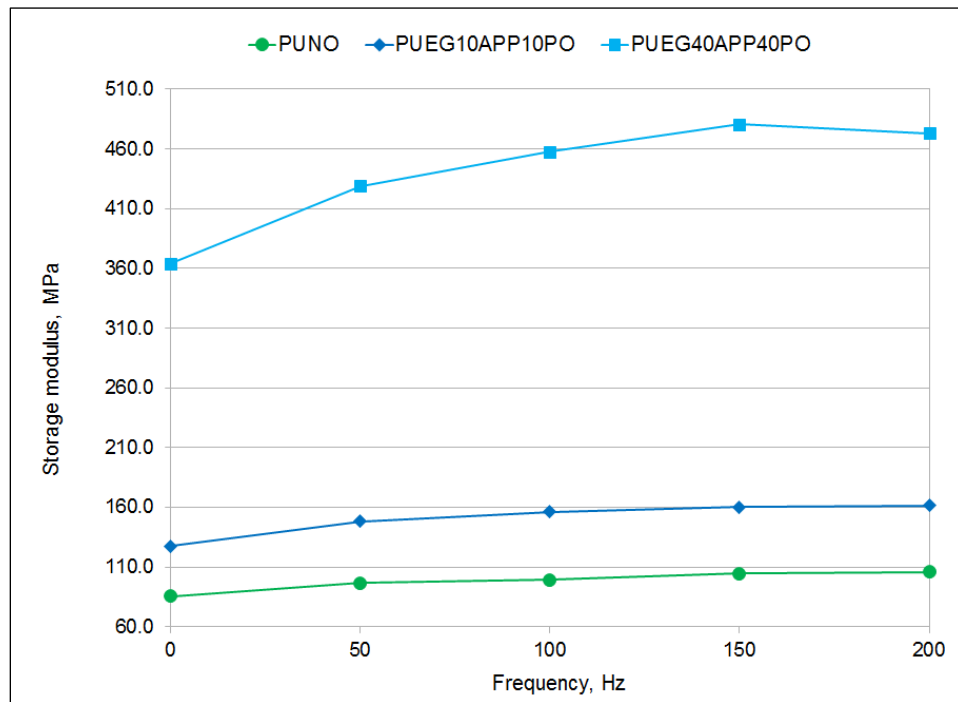


Figure 7: DMA Frequency Sweep Test Results for PUNO and PM POSS Nanocomposites



**Figure 8: DMA Frequency Sweep Test Results for PUNO and (PM+AM) POSS Nanocomposites**



**Figure 9: DMA Frequency Sweep Test Results for PUNO and Expandable Graphene + Ammonium Polyphosphate Nanocomposites**



The storage modulus for each material varies with the amount of nanofiller in the nanocomposite, see Figure 4-Figure 16. The storage modulus trend variation with respect to the amount of nanofiller is maintained at all loading frequencies. During DMA testing, the materials are subjected to extremely low strains within the elastic limits of the material; there is a similar trend in the materials' response with respect to nanofiller content observed in the initial portion of the tensile testing curves, shown in Figure 10 - Figure 15

**Figure 15.** This indicates that the material storage modulus represents the materials' behavior at low strains within the elastic limits, not the materials' response at the materials' ultimate load capacity.

For all composite materials, except PUEG40APP40PO, the storage modulus is not modified significantly, even with higher concentrations of nanofillers; see Figure 4-

Figure 9. In the case of PUEG40APP40PO, the observation is that increased nanofiller content causes the load bearing mechanism of the composite to change. This change causes the majority of the applied load is carried by the nanofiller reinforcement, and the PUNO to operate only as a binding agent. However, for all other materials the load sharing mechanism appears to work as the primary load bearing component of the nanocomposite. The low amount of nanofiller increases the materials' stiffness through the hindrance of the polymer chain motion during the deformation.

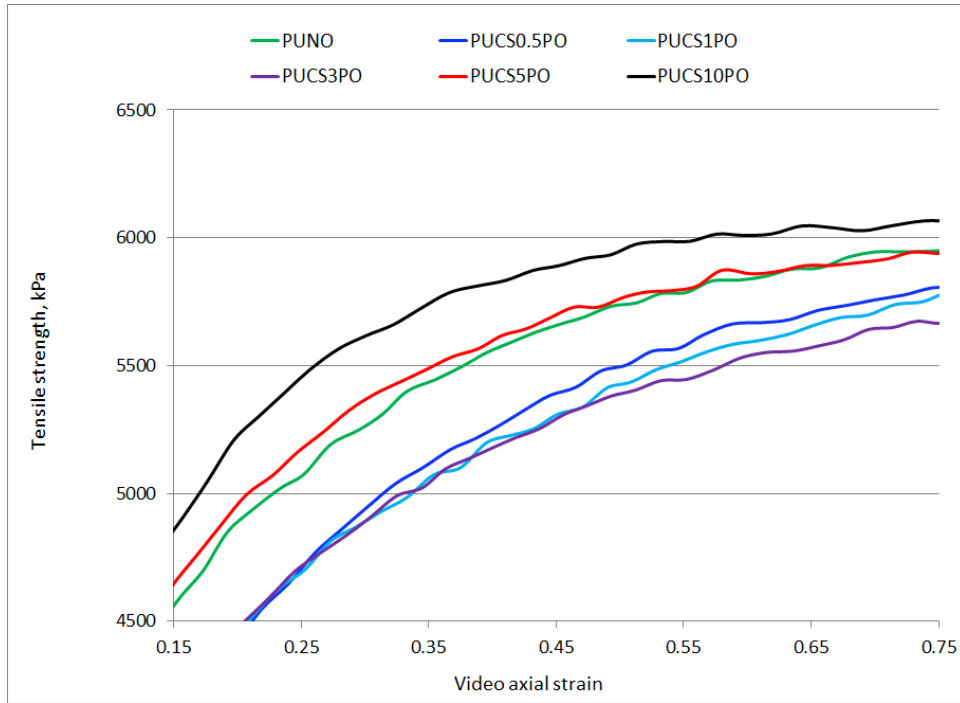


**Figure 10: Low strains tensile response of PUNO and CS nanocomposites**

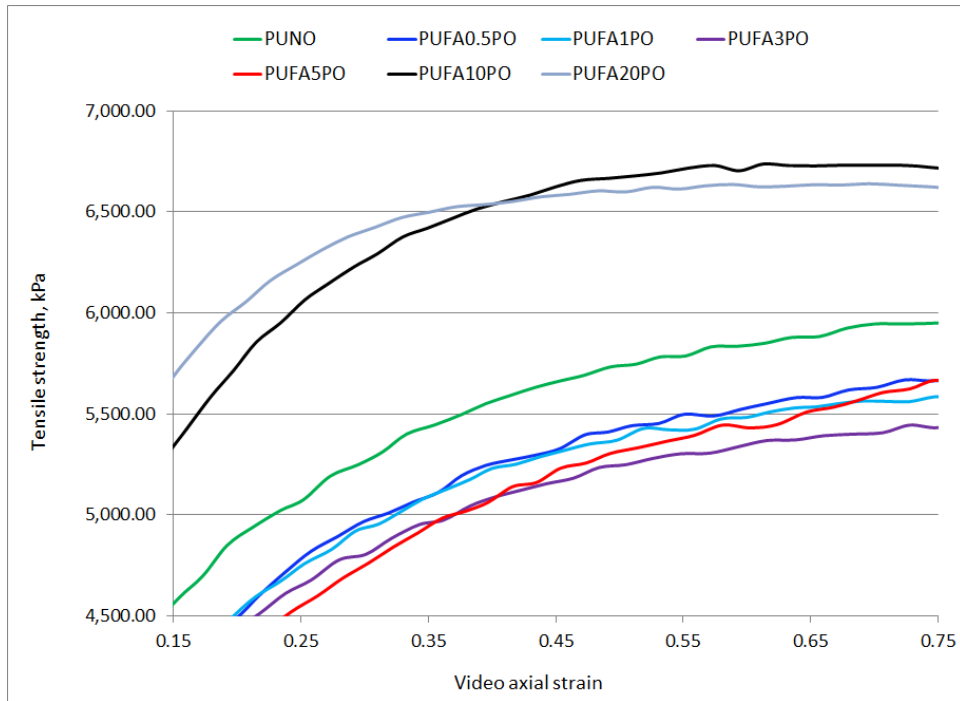


**Figure 11: Low strains tensile response of PUNO and FA nanocomposites**

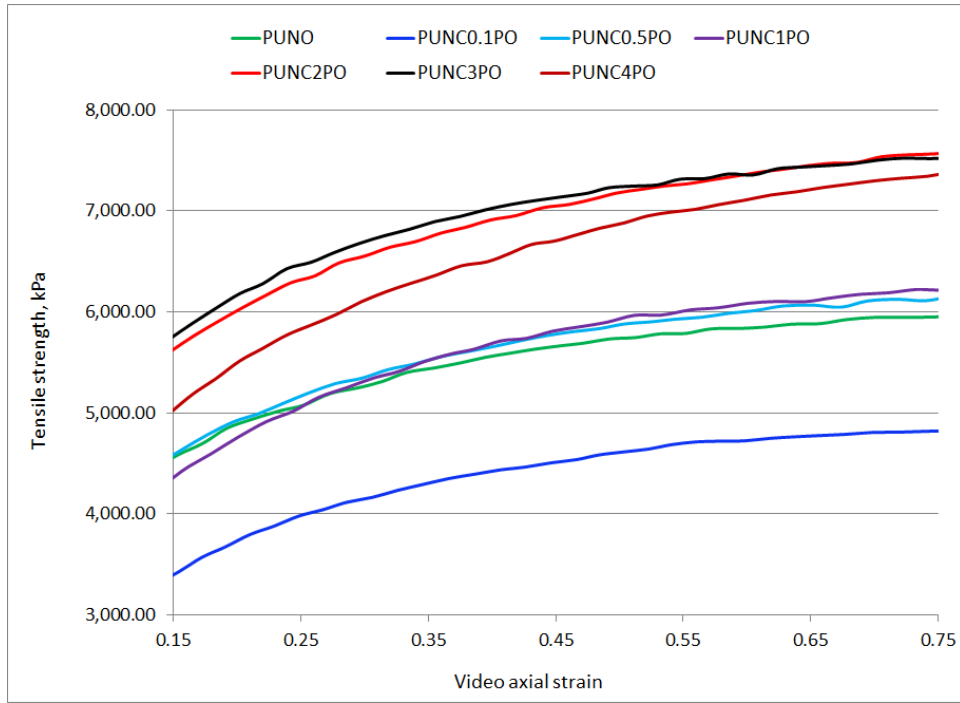


**Figure 12: Low strains tensile response of PUNO and NC nanocomposites**

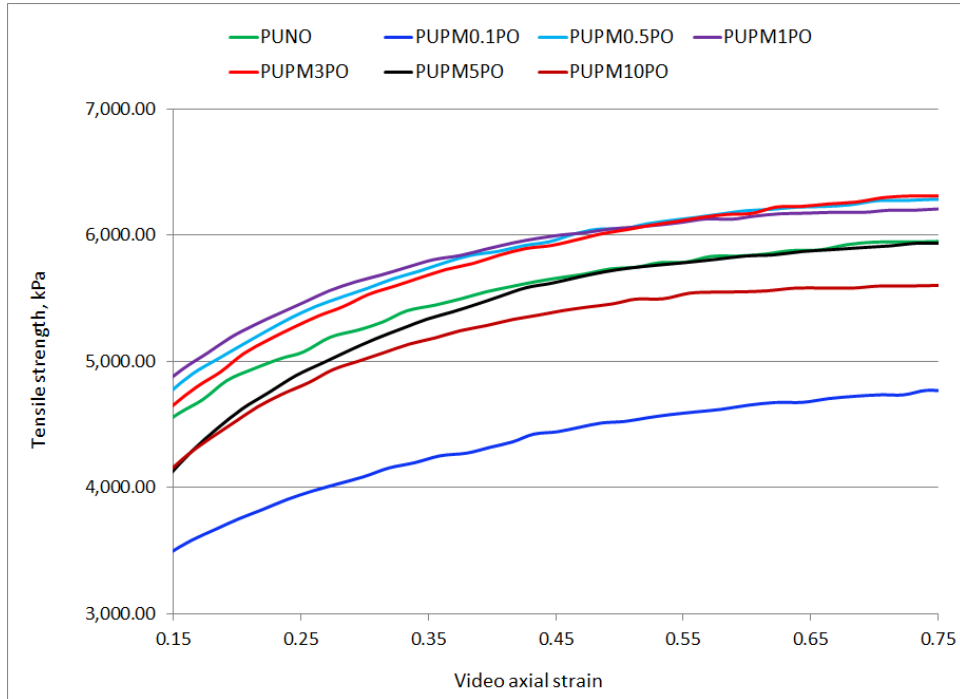


**Figure 13: Low strains tensile response of PUNO and PM POSS nanocomposites**

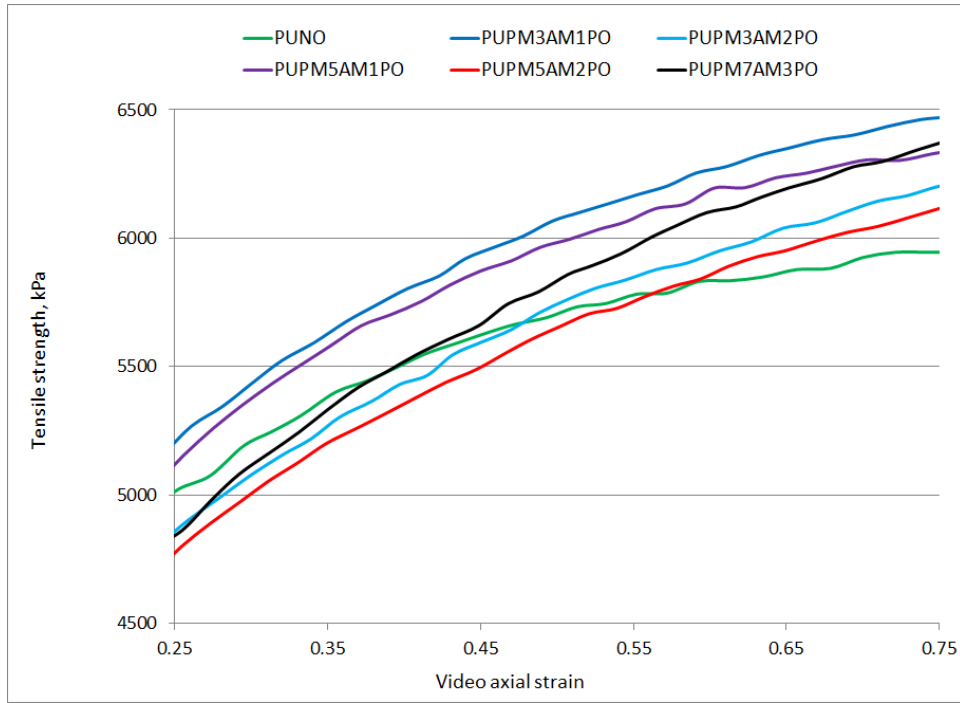


**Figure 14: Low strains tensile response of PUNO and (PM+AM) POSS nanocomposites**

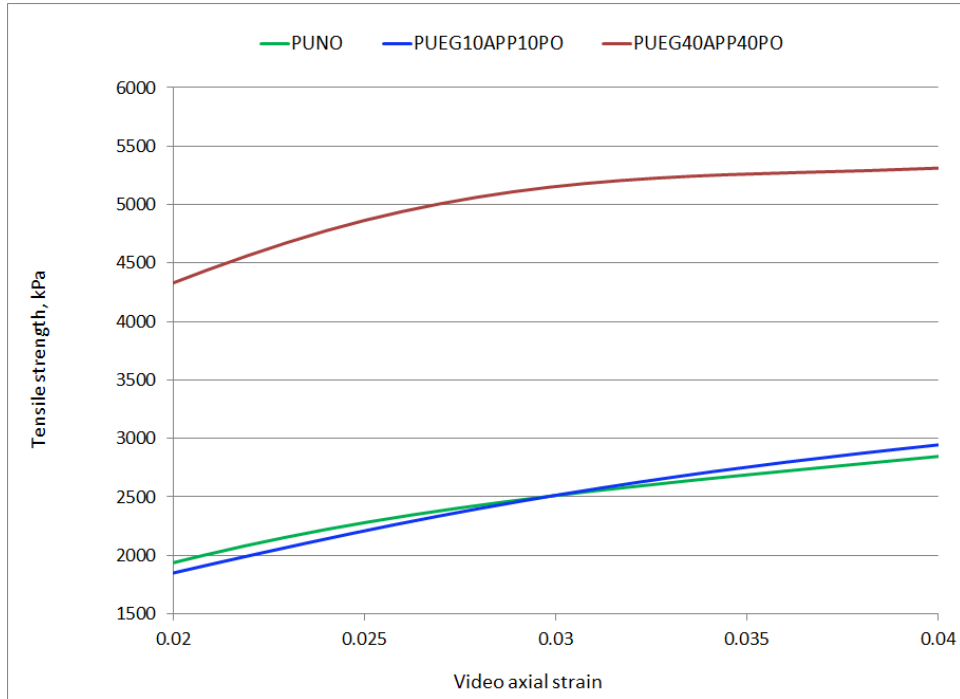


**Figure 15: Low strains tensile response of PUNO and EG + Ammonium polyphosphate nanocomposites**

Table 1 contains a list of the best performing nanocomposites in each class. A comparison of DMA results for the best performing samples in each class is plotted in Figure 16.

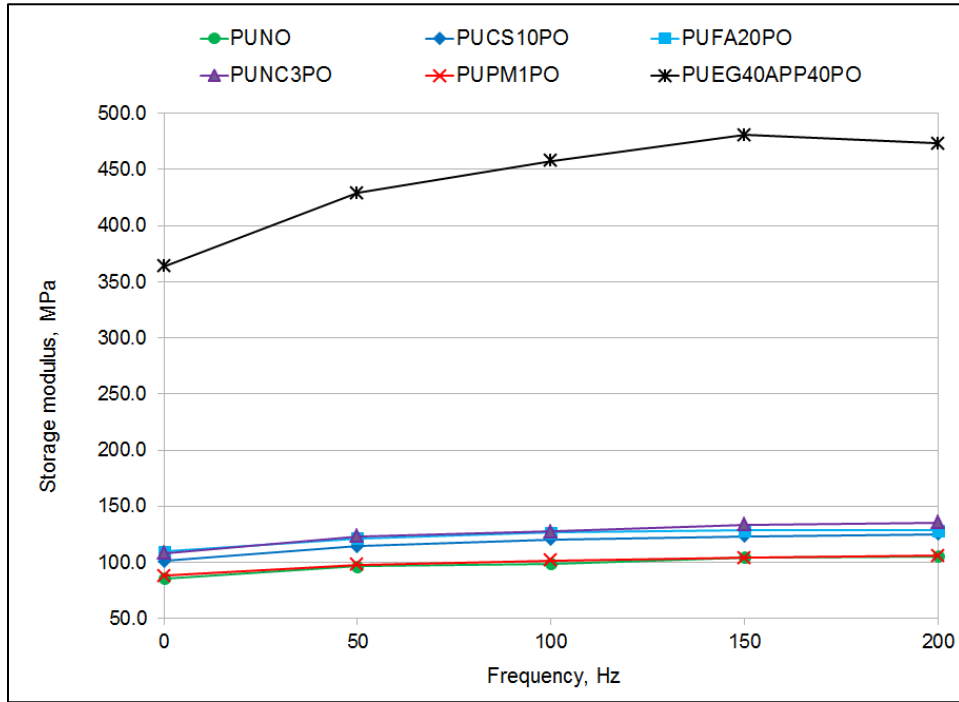


**Figure 16: Summary of DMA testing results for Polyurea nanocomposites**

**Table 1: List of nanocomposites with best DMA properties in each class**

Name of nanofiller	Best composition	Amount of nanofiller (phr)
Calcium sulfate	PUCS10PO	10
Fly ash	PUFA3PO	20
Nano clay	PUNC3PO	3
PM POSS	PUPM1PO	1
EG+APP	PUEG40APP40PO	40+40

Another parameter that is calculated during the frequency sweep is the  $\tan\delta$ . The  $\tan\delta$  values for the nanocomposites are shown in Figure 17 – Figure 22 as a function of the loading frequencies. In these figures it is apparent that the  $\tan\delta$  values practically double as the loading frequency increases from 1 Hz to 200 Hz. An explanation for this behavior is that as the loading frequency increases the material nature changes. These material changes indicate the material is strain dependent. As the frequency increases the viscoelastic material primarily behaves as an elastic material. At low frequencies, a larger amount of energy is dissipated for the polymer chain spatial rearrangement. However, at higher frequencies, the polymers do not have sufficient time for spatial rearrangement, and a large of amount of energy as dissipated as heat leading to higher values of  $\tan\delta$  at higher frequencies.

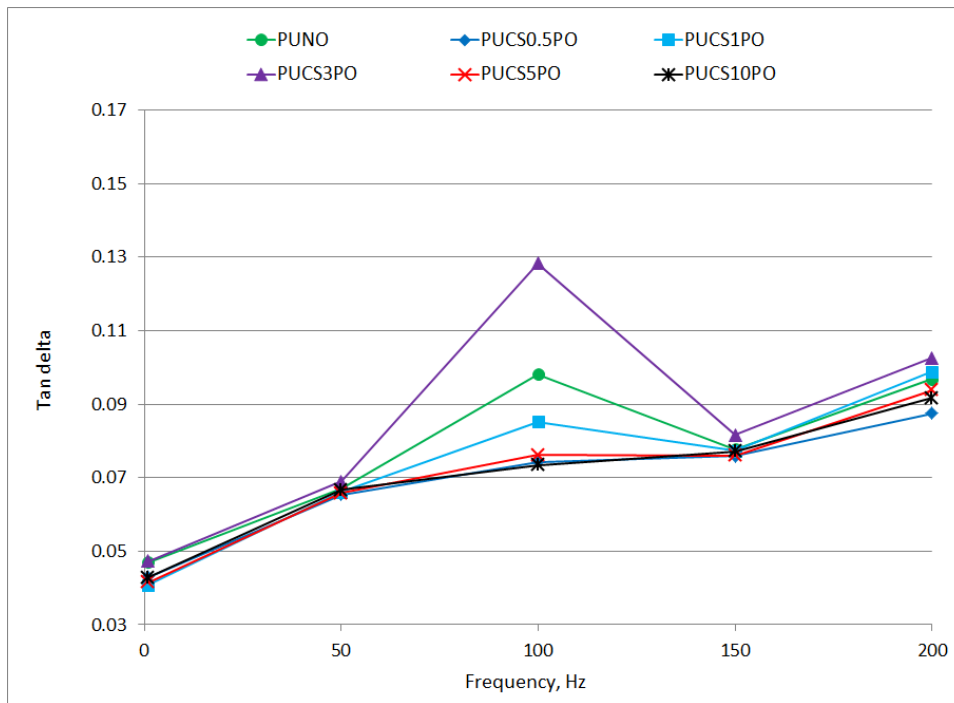


**Figure 17:  $\tan\delta$  variation during DMA testing for PUNO and calcium sulfate nanocomposites**

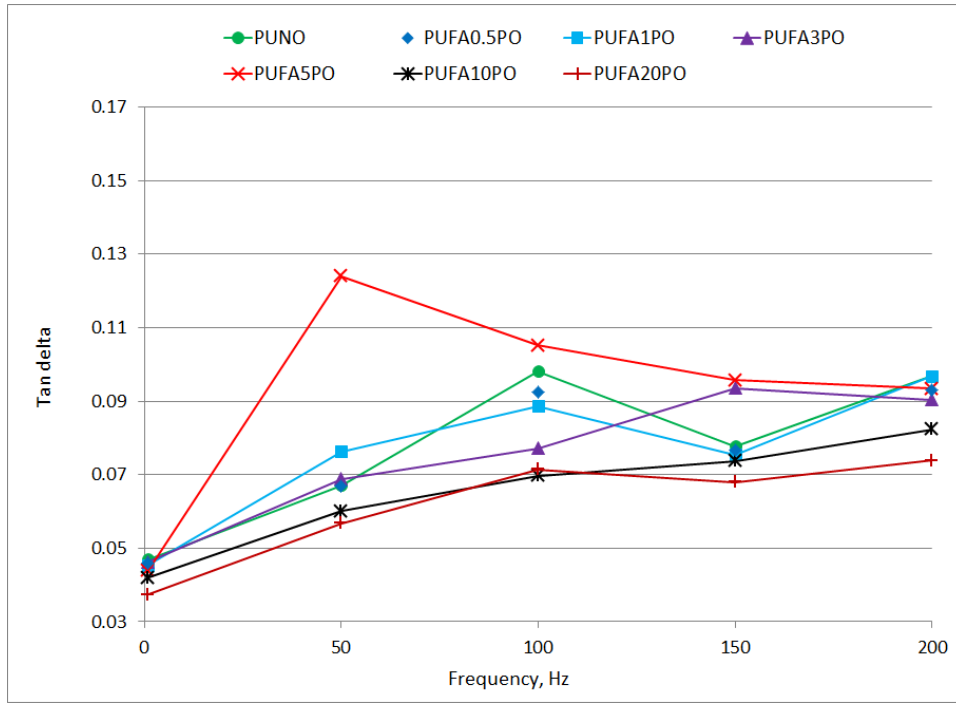


**Figure 18: Tan δ variation during DMA testing for PUNO and fly ash nanocomposites**

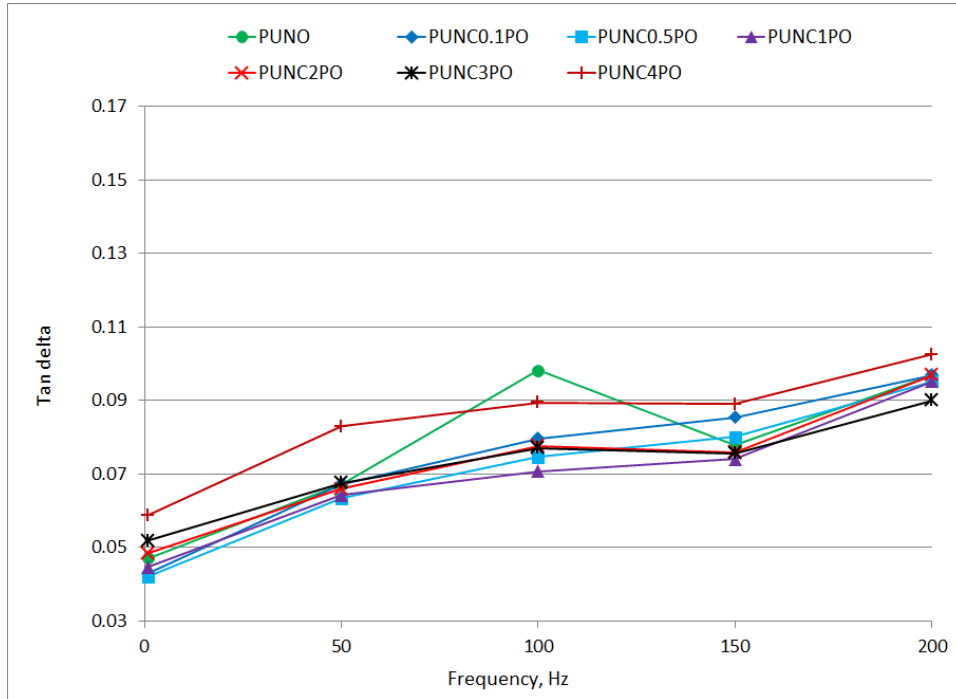


**Figure 19: Tan δ variation during DMA testing for PUNO and nanoclay nanocomposites**

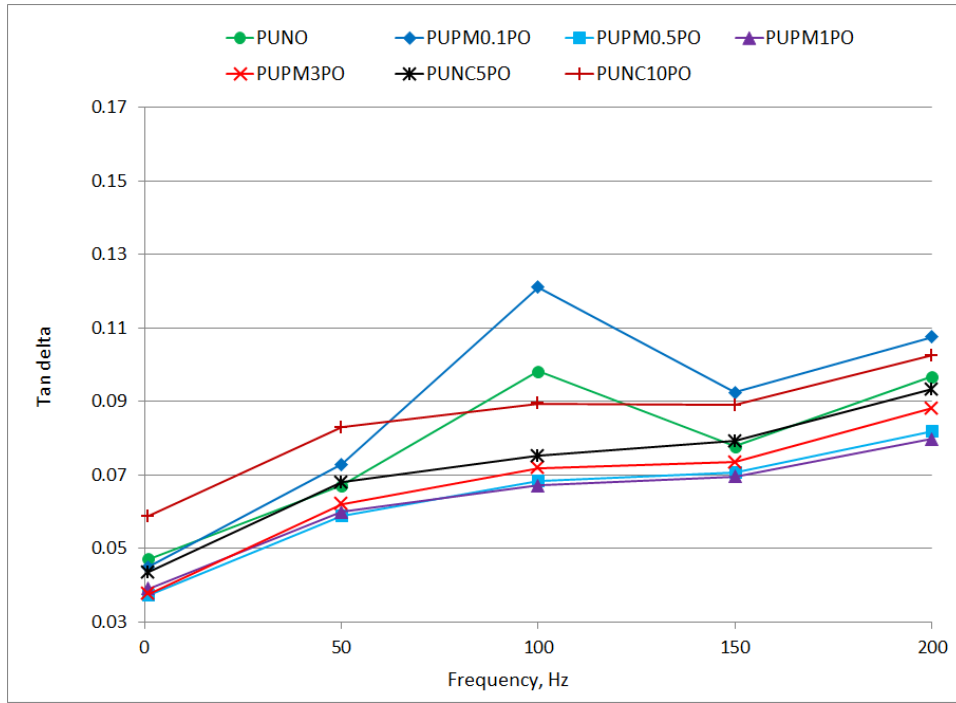


Figure 20: Tan δ variation during DMA testing for PUNO and PM-POSS nanocomposites

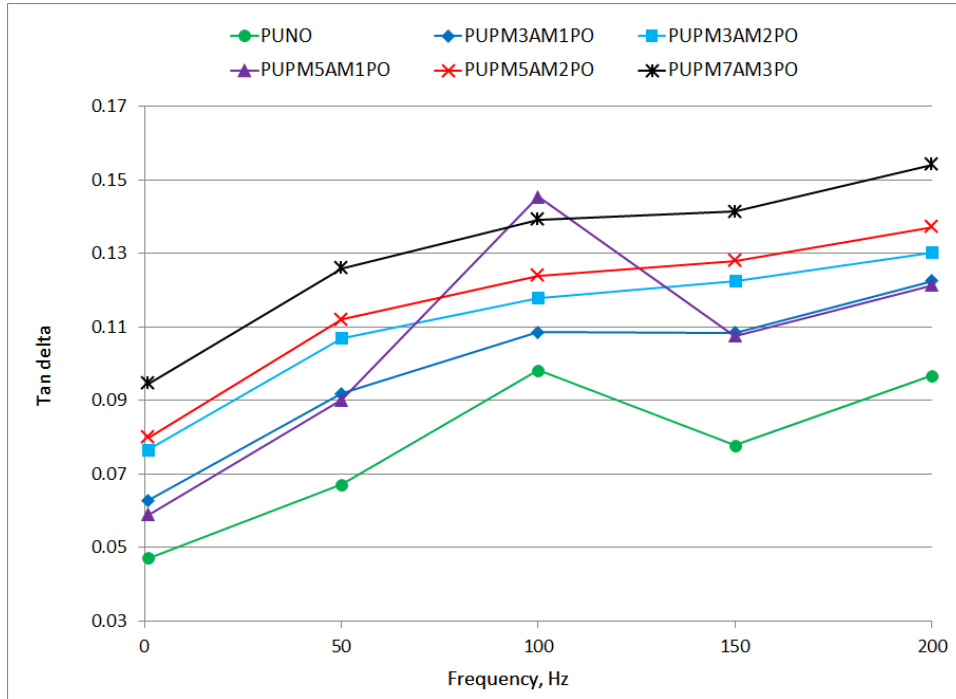
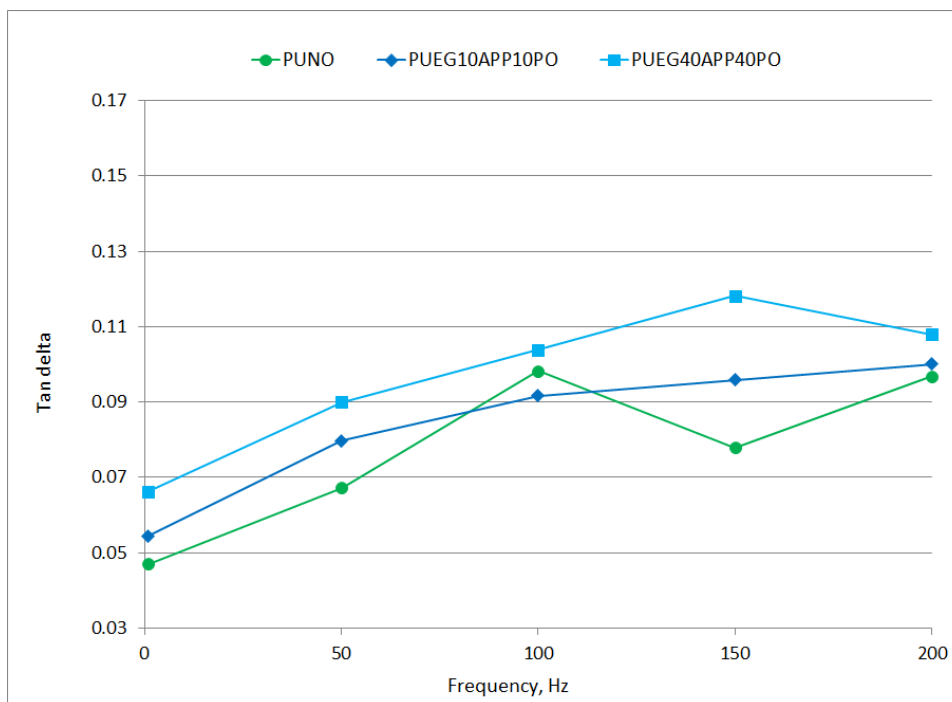


Figure 21: Tan δ variation during DMA testing for PUNO and (PM+AM) POSS nanocomposites





**Figure 22: Tan $\delta$  variation during DMA testing for PUNO and Expandable graphite + Ammonium polyphosphate nanocomposites**

For the case of calcium sulfate and PUNO nanocomposites, there is no significant change in the tan $\delta$  values as the nanofiller content is increased, see Figure 17. For fly ash and PUNO nanocomposites, the tan $\delta$  values remain the same at low nanofiller content. However, the tan $\delta$  values tend to decrease at the nanofiller content increases, see Figure 18. A decrease of 12%-27% at various frequencies is observed in the containing 20phr fly ash content. For the nanoclay and PUNO nanocomposites, the tan $\delta$  values increase for larger concentrations (3phr and 4phr) at low frequencies, see Figure 19. The maximum increase in the tan $\delta$  value is 25% in the material containing 4phr nanoclay. However, the gain in the tan $\delta$  values decreases at higher frequencies. A similar trend of higher tan $\delta$  values at higher filler contents (5 phr and 10 phr) is observed in case of PUNO and PM-POSS nanocomposites, see Figure 20.

In case of PUNO composite with different amounts of PM-POSS and AM-POSS mixture,  $\tan\delta$  values increase with increase in total filler loading (total phr of PM-POSS and AM-POSS) for all frequencies, see Figure 21. This change in  $\tan\delta$  value is more pronounced at low frequencies and it decreases as frequency is increased. At frequency of 1 Hz,  $\tan\delta$  value for PUPM7AM3PO is twice the  $\tan\delta$  for pure PUNO. However, the same ratio drops to 1.6 at the loading frequency of 200 Hz. In the same manner,  $\tan\delta$  values increase with both filler content and loading frequency for composites PUNO and different amounts of expandable graphite and ammonium polyphosphate as shown in Figure 22.

## IV. MATERIAL MULTIFUNCTIONALITY

Material multi-functionality refers to the development of a material that possesses an optimal response to various demands which may have been previously unachievable. Optimal multi-functionality is achievable for materials that are comprised of several components like composites. By altering the amount of the components an optimal material response to differing demands can be obtained, which in turn achieves the desired multi-functionality (Salonitis et al. 2010).

### **4.1 Multi-functionality for Blast and Fire Loading**

The materials being researched in this thesis are nano-polymer reinforced composites (NPRC). The multi-functionality is being utilized to meet the demands primarily created by blast and fire loading. The research to meet these loading demands is being performed at the component level. The properties of the material and the structural components are investigated as the structural component responses to each demand.

More than nineteen NPRC are evaluated in this research, see Table 2. Four materials (PUNO, PUPM3PO, EG10APP10PO with PUPM3PO, and BF) are evaluated under high fidelity blast loading using a ¼<sup>th</sup> scale set up. The

materials' response to fire testing in terms of the multi-functionality is shown in Figure 23 and Figure 24.

**Table 2: Polyurea Nano-Composites Layers Coated on ¼ scale blocks for Fire Test**

Abbreviation	Description of Material
PUNO	Pure polyurea (PU) without any filler
PUPM0.5EG10APP10PO	Two layers of PU filled with PM1285 (0.5 phr) coated with PU filled with EG (10 phr) and APP (10 phr)
PUPM0.5EG40APP40PO	Two layers of PU filled with PM1285 (0.5 phr) coated with PU filled with EG (40 phr) and APP (40 phr)
PUCS1PO	PU filled with 1 phr calcium sulfate
PUCS5PO	PU filled with 5 phr calcium sulfate
PUCS10PO	PU filled with 10 phr calcium sulfate
PUFA5PO	PU filled with 5 phr FA
PUFA10PO	PU filled with 10 phr FA
PUFA20PO	PU filled with 20 phr FA
PUNC1PO	PU filled with 1 phr NC
PUNC2PO	PU filled with 2 phr NC
PUNC4PO	PU filled with 4 phr NC
PUPM0.5PO	PU filled with 0.5 phr PM
PUPM3PO	PU filled with 3 phr PM

PUPM5PO	PU filled with 5 phr PM
PUPM10PO	PU filled with 10 phr PM
PUPM3AM2PO	PU filled with POSSes of 3 phr PM and 2 phr AM
PUPM7AM3PO	PU filled with POSSes of 7 phr PM and 3 phr AM

The parameters that are employed for multifunctionality evaluation are peak heat release rate (PHRR), energy at the break, and tensile at the break. PHRR is determined based on heat release rate (HRR) curves. These curves are obtained from cone calorimeter testing in which the samples are exposed to 50 kW/m<sup>2</sup> incident flux with an exhaust flow of 24 L/s. PHRR is defined as the highest point on the HRR curve for each material. The tensile strength and energy at break are determined through tensile testing using the Instron machine. The tensile strength is recorded by the machine as the maximum load strength, and the energy at break is recorded as the total energy consumed to break the specimen.

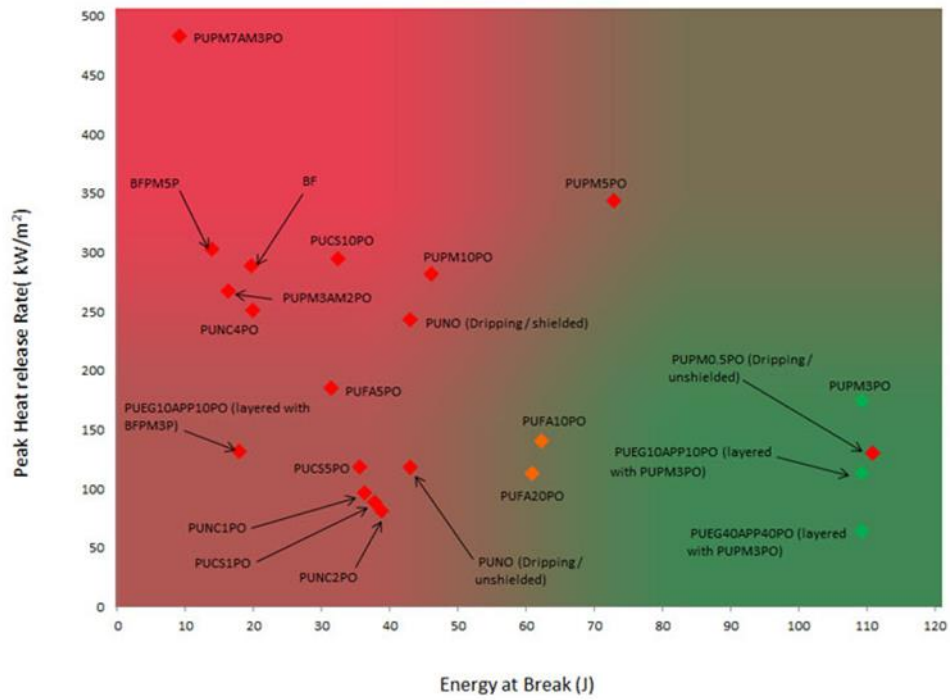
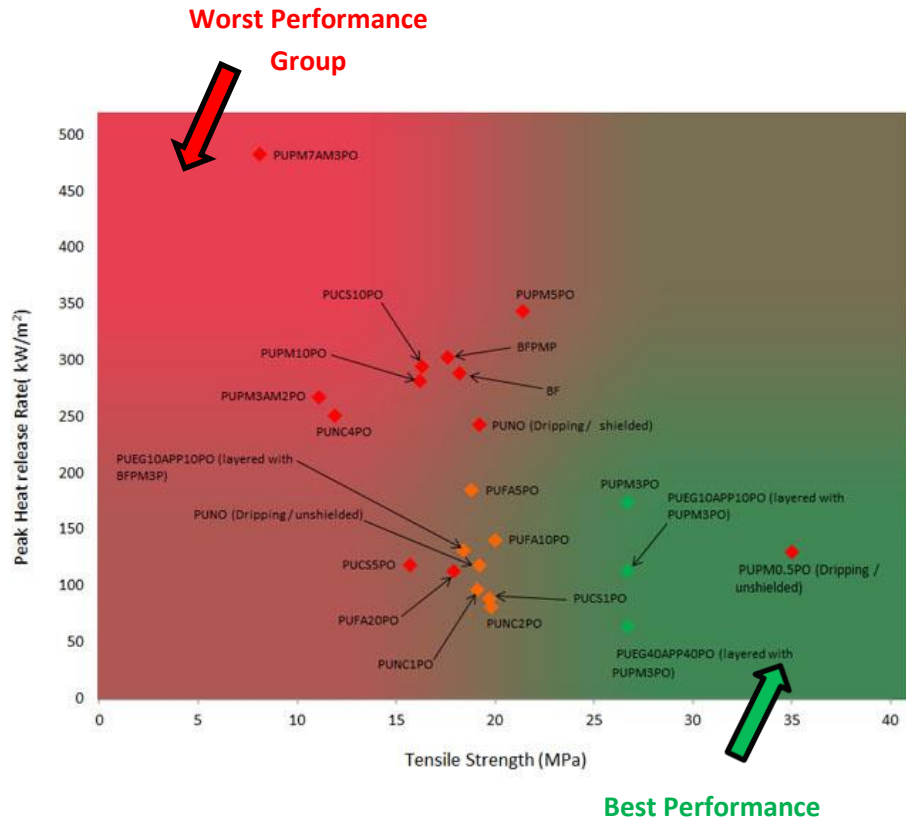


**Figure 23: Multi-functionality Performance of Selected Nano-composites**

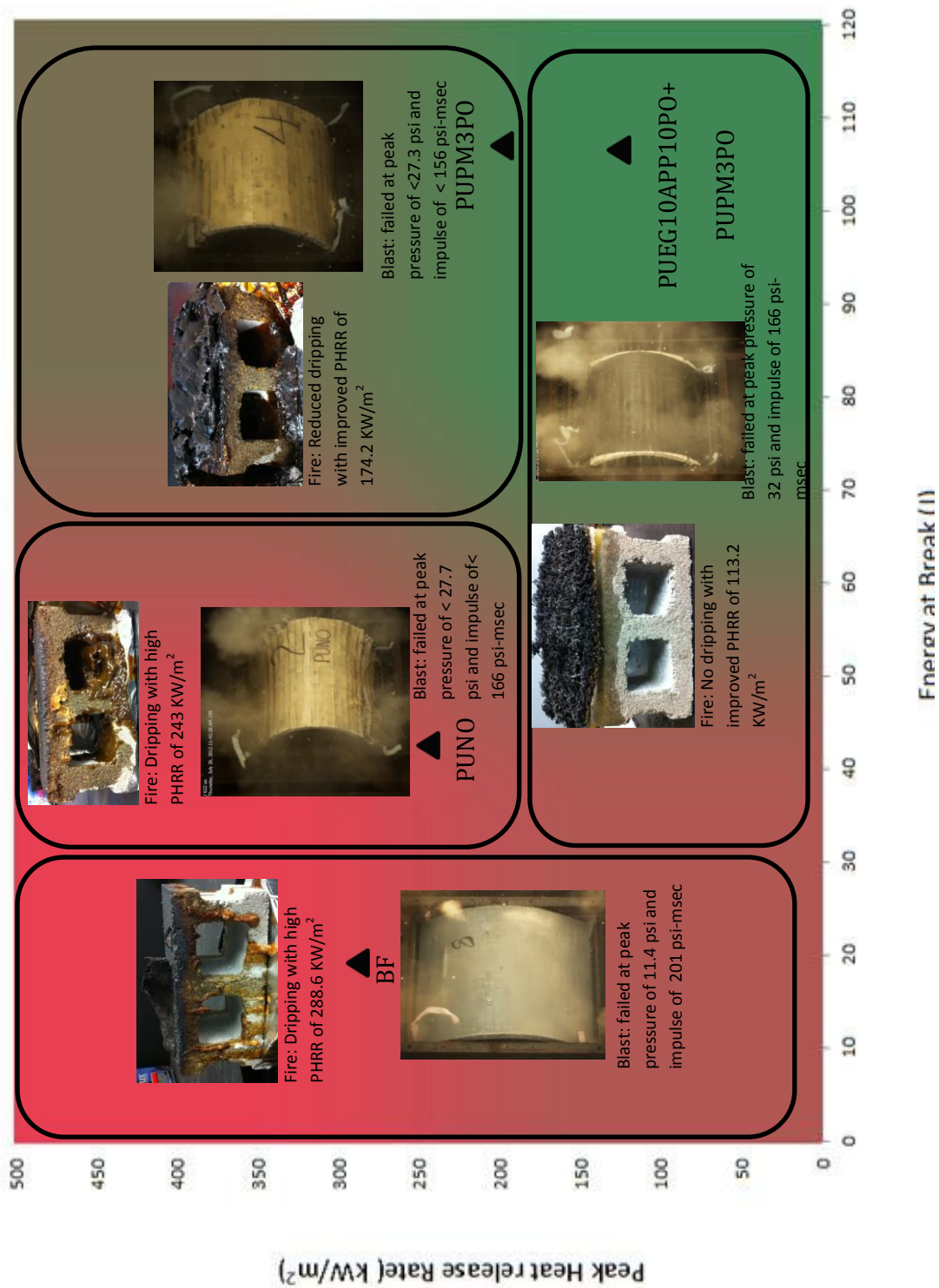


Figure 24: Validation of Multi-functionality performance of selected nanocomposites using blast and fire tests.

Based on the results of Figure 23 and Figure 24 the three materials are selected for blast testing based on their multi-functionality, include: PUPM3PO,

EG10APP10PO layered with PUPM3PO, and PUNO. PUPM3PO and the two layer system are chosen based on their multi-functionality, and the PUNO is chosen as the baseline material for comparison.

#### 4.2 Multi-functionality Index of NPRC

The multi-functionality index is a means to quantifiably compare the multi-functionality of a given material. For the method to be objective it needs to be independent of scale, while being performed on a given scale. Three scales are used in this research; these include: the constitutive model scale, structural component scale, and structural system scale. Equation 1 gives the formula used to calculate the multi-functionality index (MI). For this equation  $i^{\text{th}}$  is the demand on the material, and  $j^{\text{th}}$  is the scale, where  $i=1,2,3, \dots,N$  and  $j=1,2,3$  a relative performance criteria of the material,  $R_{ij}$ .

$$MI_j = 10 \left( \frac{\sqrt{\sum_{i=1}^{i=N} (R_{ij})^2}}{\sqrt{N}} \right)$$

#### Equation 1: Multi-functionality Index for the $j^{\text{th}}$ scale

Where  $0 \leq R_{ij} \leq 10$ , subjected to the following limits:  $R_{ij}=0$ , the material is incapable of resisting the  $i^{\text{th}}$  demands and for  $R_{ij}=10$ , the material is considered perfect, and appropriately resists the  $i^{\text{th}}$  demands.

A different index is computed for each specified scale of MI. For the materials to be accurately compared with one another, the MI must be computed for the same N value. The higher the value of MI the more demands the material is capable of resisting.



To evaluate the  $MI_j$  at the material scale,  $j=1$ , the following two values will be assigned for the performance criteria of  $R_{ij}$ . For the blast resistance,  $i=1$ , and  $R_{12}=[1, 5] \Big|_{\varepsilon(\max)} + [1,5] \Big|_{\sigma(\max)}$  is assigned. For fire resistance,  $i=2$ ,  $R_{22}=[1,10]$  for cases of non-dripping materials and  $R_{22}=[1,5]$  of dripping materials are assigned.

$MI_1$  for nineteen materials is shown in Figure 25. Based on the results presented in Figure 25, material 19 has the highest MI based on blast and fire resistance. However, material 19 is has a lower workability than material 18 particularly in terms of curing time. These limitations for material 19 would make it difficult to undergo technology transformation from the labs to practical applications.

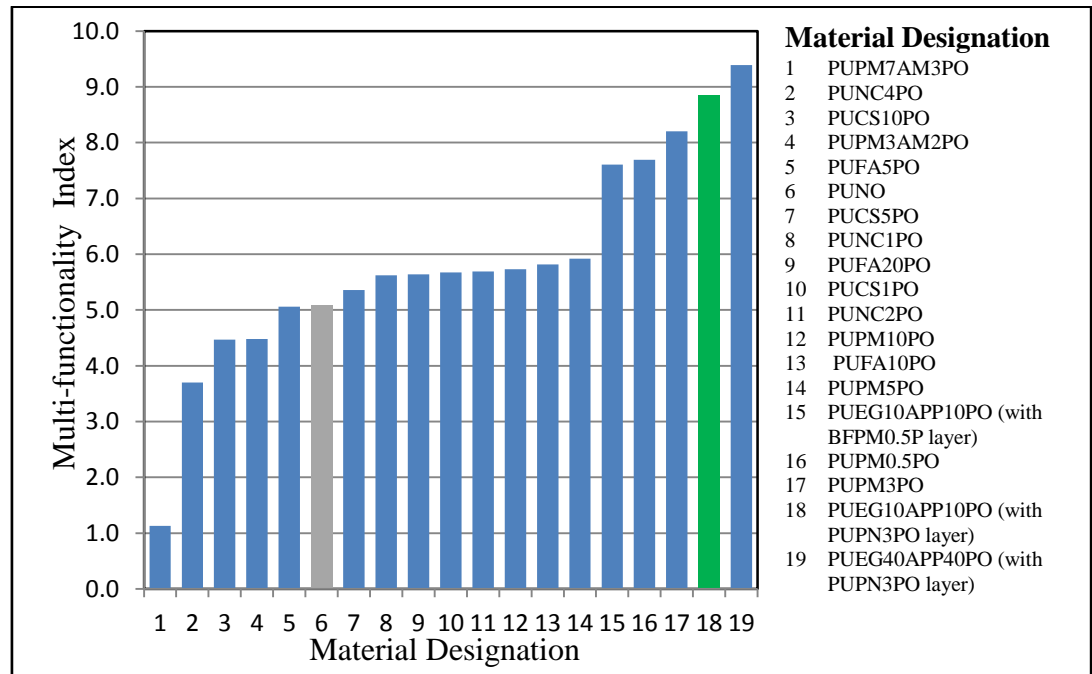


**Figure 25: Multi-functionality for Various Nano-enhanced Polymeric Materials**

## V. DETAILED EVALUATION OF MATERIALS

### 5.1 Experimental Setup

All test specimens are constructed from ¼-scale CMU blocks having dimensions of 115 mm wide, 57 mm thick, and 54 mm tall. Each wall is 1066.8 mm wide and 1460.6 mm tall and consisted of 23.5 blocks in height, with a total of 9 blocks in width. The walls are constructed in a steel sub-frame that supported the wall during construction, polyurea application, transport, and installation into the shock tube support frame.

A total of six wall specimens are tested in the research, with three different types of modified polyurea sheeting and a commercial spray applied polyurea used for retrofitting the masonry walls. A list of polyurea sheet materials used in the program is provided in Table 3 along with descriptions of the sheets. A list of test specimens included in the test program is provided in Table 4. All of the materials described in Table 4 are one layer systems except PUPM3PO+EG10APP10PO. This material is a two layer system, which contains a base layer of EG10APP10PO which is a fire retardant material and a second layer which is PUPM3PO for blast resistance. This system was developed in an effort to improve the fire resistance capabilities of the PUPM3PO material when subjected to blast loading.

**Table 3: Polyurea Sheet Materials**

Material Designation	Description	Thickness
PUNO	VP1000 (PU) without any filler	2 mm
PUPM3PO	PU filled with 3 phr POSS of PM1285	2 mm
PUPM3PO+EG10APP10PO	Two layers of PU filled with PM1285 (3phr) plus PU filled with EG (10 phr) and APP (10 phr)	4 mm
Spray Applied	Polyurea	2 mm

**Table 4: Test Specimen Description**

Test Specimen	Tests Performed	Sheet Material	Adhesive	Clamping Screws
1	1	PUNO	Loctite 375	Exposed
2	2	PUNO	Loctite 375	Exposed
3	3	PUPM3PO+EG10APP10PO	Loctite 375	Exposed
4	4	PUPM3PO	Loctite 375	Recessed
5	5-7	PUPM3PO+EG10APP10PO	Polyurea	Recessed
6	8	Spray Applied	NA	Recessed

The sheets are clamped to the supports by an Hallow Square Steel (HSS) 50.8 mm  $\times$  101.6 mm  $\times$  6.35 mm (2"x4"x 1/4") structural tubing attached to the supports with 1/4-inch diameter self-drilling screws at three inches on the center along the width of the wall. The tubes are provided in order for the top and bottom courses of CMU blocks to bear on the tubes. In the initial three tests, the screws are applied through the tube such that the screw heads are exposed at the top of the tube. In the remainder of the tests, access holes are drilled in the top surface for screw installation through the bottom surface, thus recessing the screw heads inside of the tube. Figure 26, shows one of the retrofitted wall specimens. Figure 27, shows the clamping tube at the bottom support which is similar to the top support. All but one wall is retrofitted by applying a sheet of polyurea to the non-loaded face of the CMU.

The polyurea sheet is adhered to the masonry with adhesive and clamped to the steel sub-frame at the top and bottom of the wall. Adhesion of the sheet to the wall on Specimen 1 is relatively poor, with several large bubbles in the sheet noted prior to the test. The general adhesion of the sheets to the masonry is improved for Specimen 2, 3, and 4, but some minor bubbles are noted.



**Figure 26: Test Specimen with Applied Polyurea Sheet**



**Figure 27: Bottom Tube Clamping Polyurea Sheet**

## 5.2 Experimental Analysis

A simple analytical model was developed by BakerRisk to aid in the selection of an initial test load for Specimen 1. The intent was to utilize an existing moment-curvature flexural model containing a secondary membrane response to develop a resistance deflection function for each upgraded wall system. However, when applying this model, it is found that the material properties of the PUNO sheets are very different from the material properties of the typical polyurea materials for which the model is developed. That being that case, the result is very little flexural capacity of the wall. Therefore, it is determined that the most expedient approach is to generate a resistance function based on the membrane response of the sheet as the only mode of response for the wall. A resistance function is determined for the PUNO sheet, given the dimensions and support conditions of the wall. This resistance function is input into a general single-degree-of-freedom spreadsheet tool to develop pressure-impulse (P-I) diagrams for the wall for several limit states. The resistance function is determined by using the equation shown in Equation 2. The resulting P-i diagrams for a ductility ratio of 0.5, 0.75, and 1.0 are provided in Figure 6. Based on the analysis, a 206.8 kPa pressure load with an impulse of 1379 kPa-ms is selected as the initial test load. The load is selected based on the P-i diagram for a ductility ratio of 0.75, as well as previous test loads for previous tests performed by Irshidat et al. (2011).

$$r_u = 64E \left( \frac{t}{3L^4} \right) d^3$$

**Equation 2: Resistance Function for PUNO**

Where  $r_u$  is the unit resistance,  $E$  is the elastic modulus,  $t$  is the thickness of sheet,  $L$  is length of span, and  $d$  is the deflection at mid-span.

The analysis approach is not adjusted based on observed test results and is not intended to be used for future analysis of similar wall systems. Based on the initial test, it is assumed that the estimate is reasonable, but that some effects due to interaction between the sheet and CMU block may affect the allowed elongation of the sheet. Further selection of test loads is based on observed responses in completed tests. Upon completion of the work, it is evident that a more detail analytical approach is necessary to properly predict the response of masonry walls upgraded with polyurea sheet materials.

Figure 28, shows a Pressure-Impulse (P-I) diagram for Test Specimen 1. This diagram can be used to predict the point at a wall with a similar coating will fail based on a given pressure and impulse. The points on each curve mark the maximum loading it can take before complete failure. All points below the curve are considered unfailed and all points above are considered to be in failure. This type of diagram is utilized to determine the potential stability of a structure during a blast loading or in this case determine the loading an individual structure can with stand. A P-I diagram is typically only accurate when used for a similar structure and retrofit system.

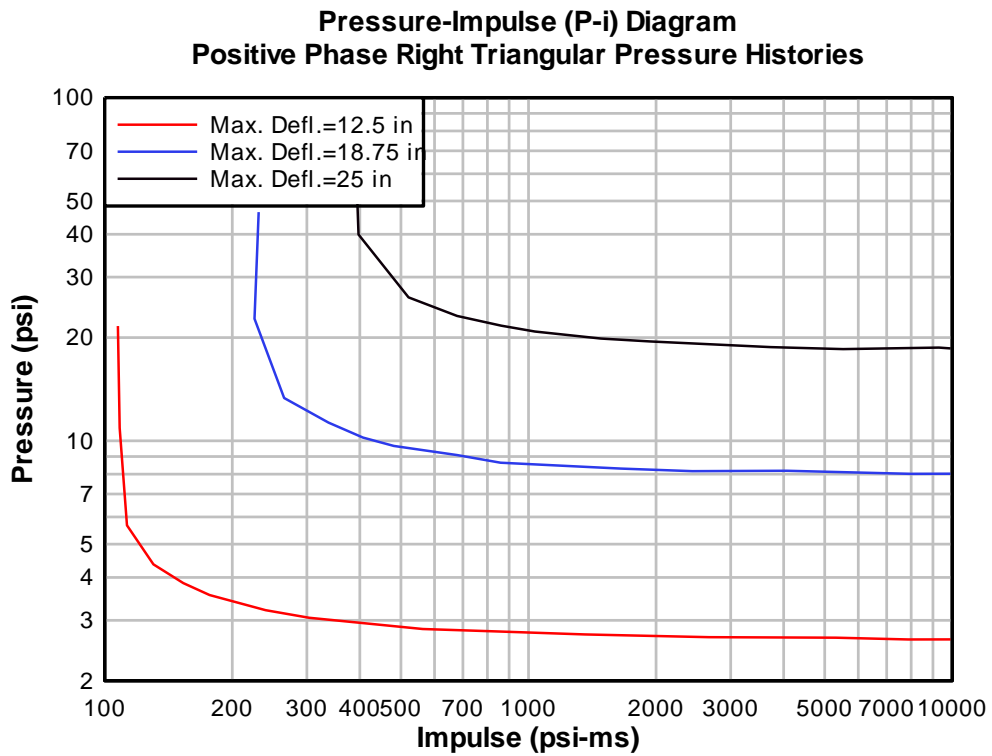


**Figure 28: Estimated P-I Diagrams for Test Specimen 1**

### 5.3 Experimental Test Results

Testing is conducted in the BakerRisk shock tube. Test instrumentation included three pressure transducers mounted in the walls and floor of the shock tube at the target end to measure the applied load in each test. High-speed cameras and a fixed grid are used to gather specimen displacement data in all tests. All tests are documented using still photography, video, and high-speed video from two view angles. A total of 8 tests are conducted on the 6 specimens. A summary of the tests are provided in Table 5. Discussion of the results of each test is provided in the following paragraphs.

**Table 5: Summary of Test Results**

Test	Test Specimen	Peak Pressure (kPa)	Applied Impulse (kPa-ms)	Response Description
1	Specimen 1	242.7	1296	Sheet failure, tearing occurred at 850.9 mm of deflection, majority of debris within 6 m.
2	Specimen 2	191.1	1145	Sheet failure, tearing occurred at 533.4 mm of deflection, majority of debris within 12.2 m.
3	Specimen 3	220.6	1145	Inspection of sheet revealed thin areas at tear initiation points.
4	Specimen 4	188.2	1076	Sheet prevented generation of significant debris. Tearing of sheet across half of width. Debris limited to 5% of wall.
5	Specimen 5	78.6	1358	Sheet failure, tearing occurred at 558.8 mm of deflection, majority of debris within 12.2 m.
6	Specimen 5	119.3	1165	Approximately 1/3 of masonry remained adhered to sheet, remainder 12.2 m from wall.
7	Specimen 5	141.3	869	Sheet prevented generation of significant debris. Peak deflection of sheet is 317.5 mm .
8	Specimen 6	78.6	1386	Sheet prevented generation of significant debris. Approximately 10 blocks translated past edges of sheet. Peak deflection of sheet could not be determined.

### 5.3.1 Test 1 Results

The CMU wall with a PUNO sheet applied to the non-loaded face is subjected to a test load having a peak pressure of 242.7 and an impulse of 1296 kPa-ms. The test specimen responded to the applied load with the masonry wall cracking at every mortar joint and the polymer sheet acting as a membrane until the sheet failed. A mid-span deflection of 850.9 is reached at 64 ms (ms) when tearing of the sheet is initiated. The tearing occurred at approximately four to five block courses from the top of the wall. The sheet remained attached to the bottom support. The masonry



blocks are generated as debris. Most of the masonry landed within 6 meters of the wall location but several blocks are found more than 15.24 meters from the test location.

### **5.3.2 Test 2 Results**

The CMU wall with a PUNO sheet applied to the non-loaded face is subjected to a test load having a peak pressure of 191.1 kPa and an impulse of 1145 kPa-ms. The test specimen responded to the applied load with the masonry wall cracking at every mortar joint and the polymer sheet acting as a membrane until the sheet failed. A deflection of 533.4 mm is reached at 46 ms when tearing of the sheet is initiated. The tearing occurred at approximately three to five courses from the bottom of the wall and then a second tear occurred at the top support. Masonry debris is generated with blocks thrown more than 18.3 meters. The bulk of debris is evenly distributed within 12.2 meters from the test location.

### **5.3.3 Test 3 Results**

The CMU wall with a PUPM3G10APP10PO sheet applied to the non-loaded face is subjected to a test load having a peak pressure of 220.6 kPa and an impulse of 1145 kPa-ms. The test specimen responded to the applied load with the masonry wall cracking at every mortar joint and the polymer sheet acting as a membrane. The sheet membrane deflected and retained all but 10 blocks that passed the sheet at their vertical edges or through a tear formed near the top of the specimen that extended approximately half way across the width of the wall. A deflection of 495.3 mm is reached at 52 ms when tearing of the sheet initiated. The deflection remained constant for approximately 20 ms while tearing occurred before the sheet began to rebound. Tearing occurred approximately 1.5 courses from the top of the wall (38.1

mm from the steel tube anchoring the sheet to the top support) at the left edge of the specimen. Masonry debris is generated with blocks falling to the ground from the specimen and remaining on the test structure or within 3 meters of the wall.

#### **5.3.4 Test 4 Results**

The CMU wall with a PUPM3PO sheet applied to the non-loaded face is subjected to a test load having a peak pressure of 188.2 kPa and an impulse of 1076 kPa-ms. The test specimen responded to the applied load with the masonry wall cracking at every mortar joint and the polymer sheet acting as a membrane until the sheet fails. A deflection of 558.8 mm is reached at 48 ms when it is estimated tearing near the top support initiated. Tearing occurred approximately 1.5 courses from the top of the wall at the left edge of the sheet. A secondary tear formed along the bottom support tube, with the tear initiating in the center of the wall 6 ms after the top tear initiated. The masonry blocks and sheet material are generated as debris. Individual blocks are thrown more than 18.3 meters from the wall location and are evenly distributed from wall to the extreme distance. However, approximately 1/3 of the masonry wall remained intact with the sheet material and landed approximately 6 meters from the initial wall location.

#### **5.3.5 Test 5 Results**

The CMU wall with a PUPM3PO+ EG10APP10PO sheet applied to the non-loaded face is subjected to a test load having a peak pressure of 78.6 kPa and an impulse of 1358 kPa-ms. The test specimen responded to the applied load with the masonry wall cracking at every mortar joint and the polymer sheet acting as a membrane. The sheet membrane deflected and retained all blocks. A peak deflection of 317.5 mm is reached at 62 ms. The sheet material and masonry rebounded back to

a near planar condition. The masonry is significantly damaged, with approximately 10% of the blocks removed completely from the wall, mainly along the edges, and another 10% of blocks losing the load side face shell. Most of the lost masonry is observed to remain on the loaded side of the specimen. Some partial blocks are observed to be wedged between the sheet edge and support frame and small particles of masonry debris is observed on the ground on the non-loaded side of the specimen.

### **5.3.6 Test 6 Results**

The damaged CMU wall with a PUPM3PO+EG10APP10PO sheet applied to the non-loaded face is subjected to a test load having a peak pressure of 119.3 kPa and an impulse of 1165 kPa-ms. Wall and sheet deformed under blast load, with the sheet preventing the majority of masonry from becoming debris on the protected side of the specimen. Approximately 10 blocks are observed to pass by their sheet edges to land on the ground on the protected side of the specimen. These blocks are observed within 3 meters of the specimen. All other masonry is retained on the loaded side of the wall with all but the top and bottom rows of block dislodged from the sheet and in a debris pile on the floor. Deflection data could not be gathered due to a dust cloud formed as the shock wave impacted the previously damaged masonry.

### **5.3.7 Test 7 Results**

The PUPM3G10APP10PO sheet without any remaining masonry is subjected to a test load having a peak pressure of 141.3 kPa and an impulse of 869 kPa-ms. The sheet material responded to the applied load as a membrane until tension failure of the sheet occurred. Tearing initiated at 16 ms at the right edge of the sheet at the top support and progressed across the full width of the sheet. The peak deflection of the sheet at mid-span at this time is in excess of 762 mm. The sheet remained attached to

the bottom support.

### **5.3.8 Test 8 Results**

The CMU wall with a spray applied polyurea coating on the non-loaded face is subjected to a test load having a peak pressure of 78.6 kPa and an impulse of 1386 kPa-ms. The wall responded initially in flexure with a transition to membrane response. The spray applied coating responded as a membrane until tension failure of the coating occurred. Tearing initiated at time 38 ms with tears forming at mortar joints 25.4 mm above the bottom support and 25.4 mm below the top support almost simultaneously. The mid-span deflection of the wall at 38 ms is 317.5 mm. The center section of the wall, both the coating and block, are generated as debris. Masonry debris is observed to be thrown up to 12.2 meters, but most of the block and the coating is observed to be within 6 meters of the original wall location.

## **5.4 Computational Modeling of CMU Panels Subjected to Air Blast Loading Using Finite Element Method**

To accurately study the effects blast loading has on CMU walls, and to comprehend their structural behavior under this loading condition numerous experiments are essential to obtain an appropriate amount of data for researchers to effectively analyze and process the results. However, there is great expense in performing a blast experiment which in turn places a limitation on the amount of testing that can be performed, predictably at a specified time. Due to the expense an alternative method for obtaining the results of an experiment are sought. This section will focus on the development of a computational model that can reasonably duplicate the mechanisms of wall failure and midpoint deflection for a retrofitted CMU wall subjected to blast loading. One method that has

proven efficient in both cost and time compared to performing actual experiments is Finite Element (FE) modeling. For this research a finite element model has been established in order to make experimental predictions. The ANSYS AUTODYN is chosen for this project. The program utilizes an explicit hydrocode that uses finite element, finite difference, and finite volume techniques to solve a great variety of non-linear dynamic problems. In this research ANSYS AUTODYN is used to model and analyze CMU walls, which have been retrofitted with nano-reinforced elastomeric materials, when subjected to a blast loading.

#### **5.4.1 Finite element configuration and mesh**

To replicate the experimental behavior of the system the same set up is used when creating the model. The experimental CMU wall dimensions of 24 blocks in height and 9 blocks in width are used in the finite element software AUTODYN (*AUTODYN Theory Manual* 2006). Each individual layer of the retrofitted CMU wall is represented by 11289 Lagrangian elements, 4320 are filled with a masonry material representative of the bricks and 3206 are filled with a mortar material for brick bonding. The double layer retrofitted CMU walls are represented by 15052 Lagrangian elements, 4320 bricks and 3206 are filled with a mortar material for brick bonding; with the remainder in the single and double layer system represented by the retrofit material. Figure 29 shows the geometry and mesh used for the CMU walls.

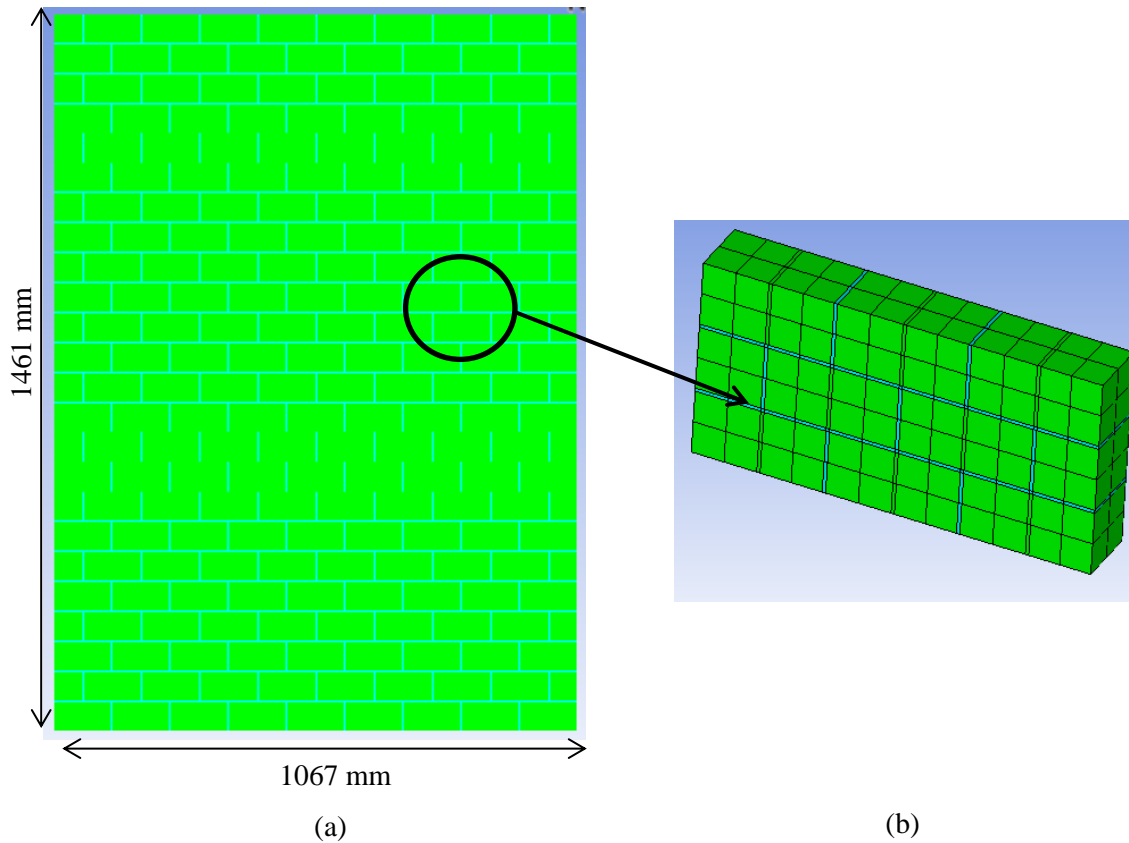


**Figure 29: a) Wall geometry (b) F.E. Mesh**

## 5.4.2 Material Models and Parameters

To model a new material in AUTODYN, the parameters of equation of state (EOS), strength model, and failure model should already be defined through manufacturer's information and/or mechanical testing of the material.

### 5.4.2.1 Unreinforced masonry

The response of masonry under shock loading is a complex phenomenon. A variety of constitutive models for the dynamic and static response of masonry have been proposed over the years. In this research, Porous equation of state (EOS), Drucker-Prager strength model, and Hydrodynamic tensile

failure ( $P_{\min}$ ) model are used to represent the unreinforced masonry. These models are discussed in details in *AUTODYN Theory Manual* (2006).

#### **5.4.2.2 Mortar**

The Compaction equation of state (EOS), MO Granular strength model, and Hydrodynamic tensile failure ( $P_{\min}$ ) model are used to represent the mortar.

#### **5.4.2.3 Nano Polymer Reinforced Elastomeric Material**

A real EOS should be defined for these new elastomeric materials; however, due to the low pressure level introduced by blast waves, a linear equation of state functions as a starting place for this study. Equation 3 shows the linear EOS used to model all three retrofitted materials.

$$P = K\mu$$

#### **Equation 3: Linear EOS for modeling all Retrofit Materials**

Whereas, K is the material bulk modulus;  $\mu$  is volumetric strain as given by Equation 4;  $\rho$  is the material density; and  $\rho_o$  is the reference density.

$$\mu = \frac{\rho}{\rho_o} - 1$$

#### **Equation 4: Volumetric Strain Equation**

Elastic strength model and principal strain failure criterion are used to model these materials. All material models used in this research are summarized in Table 6. More details are available in *AUTODYN Theory Manual* (2006).

Tables 6-11 summarize the mechanical properties and stress-strain values that are used to create the material models in AUTODYN.

**Table 6: Material Models**

Material	EOS	Strength Model	Failure Model
Masonry	Porous	Drucker-Prager	Hydrodynamic tensile failure ( $P_{min}$ )
Mortar	Compaction	Mo Granular	Hydrodynamic tensile failure ( $P_{min}$ )
PUNO	Linear	Piecewise Johnson-Cook	Plastic Strain
PUPM3PO	Linear	Piecewise Johnson-Cook	Plastic Strain
EG10APP10PO	Linear	Piecewise Johnson-Cook	Plastic strain

**Table 7: Mechanical Properties of PUNO**

Mechanical Property	Value
Reference Density (g/cm <sup>3</sup> )	1.26 E+000
Bulk Modulus (kPa)	2.57 E+006
Shear Modulus (kPa)	9.00 E+004
Specific Heat (J/kgK)	1.50 E+003
Thermal Softening Exponent	1.00 E+020
Plastic Strain	1.68
Geometric Strain	1.13
Strain Rate Constant	0.31
Reference Strain Rate (/s)	1.00

**Table 8: Stress-Strain Values for PUNO**

Effective Plastic Strain	Yield Stress (kPa)
0.000000	6.02 E+003
0.350657	8.77 E+003
0.662172	1.23 E+004
0.890768	1.61 E+004
1.061602	2.01 E+004
1.190584	2.45 E+004
1.201470	2.50 E+004
1.359402	3.36 E+004
1.501184	4.67 E+004
1.598983	6.30 E+004
1.794921	1.21 E+005



**Table 9: Mechanical Properties of PUPM3PO**

<b>Mechanical Property</b>	<b>Value</b>
Reference Density (g/cm <sup>3</sup> )	1.067 E+000
Bulk Modulus (kPa)	2.73 E+002
Shear Modulus (kPa)	2.83 E+002
Specific Heat (J/kgK)	0.00 E+000
Thermal Softening Exponent	0.00 E+000
Plastic Strain	1.90
Geometric Strain	1.50
Strain Rate Constant	0.31
Reference Strain Rate (/s)	1.00

**Table 10: Stress-Strain Values of PUPM3PO**

<b>Effective Strain</b>	<b>Plastic Yield Stress (kPa)</b>
0.000000	1.00 E+002
0.423800	1.73 E+004
0.739125	2.19 E+004
0.952936	2.60 E+004
1.144727	3.14 E+004
1.275995	3.73 E+004
1.378878	4.43 E+004
1.576510	7.55 E+004
1.666940	1.11 E+005
1.729618	1.49 E+005
1.749268	1.83 E+005

**Table 11: Mechanical Properties of EG10APP10PO**

<b>Mechanical Property</b>	<b>Value</b>
Reference Density (g/cm <sup>3</sup> )	1.15 E+000
Bulk Modulus (kPa)	3.76 E+005
Shear Modulus (kPa)	3.886 E+004
Specific Heat (J/kgK)	0.00 E+000
Thermal Softening Exponent	0.00 E+000
Plastic Strain	1.88
Geometric Strain	2.00
Strain Rate Constant	0.21
Reference Strain Rate (/s)	1.00

**Table 12: Stress-Strain Values for EG10APP10PO**

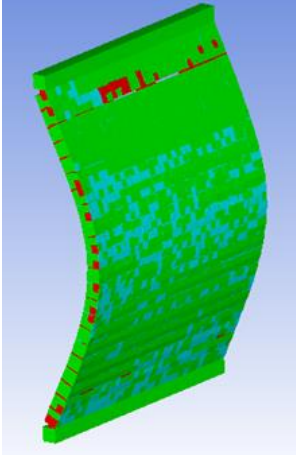
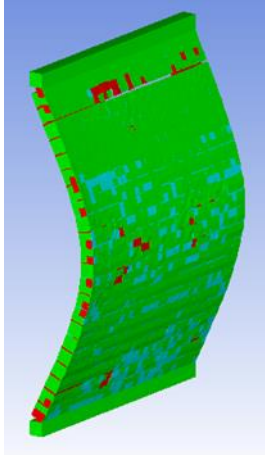


<b>Effective Plastic Strain</b>	<b>Yield Stress (kPa)</b>
0.000000	8.41 E+003
0.019965	8.52 E+003
0.318010	1.14 E+004
0.547320	1.46 E+004
0.728616	1.79 E+004
0.880322	2.17 E+004
1.002745	2.60 E+004
1.100671	3.02 E+004
1.181740	3.49 E+004
1.251674	4.00 E+004
1.345725	4.86+004

## **5.5 Numerical Simulation of Experiment Results**

### **5.5.1 Wall #1 Results**

Wall #1 is retrofitted with a single layer of PUNO that is 2 mm in thickness. The pressure of 206.8 kPa is applied to the wall using an impulse of 1144.5 kPa\* ms. Wall #1 failed at the end near the supports. The maximum midpoint deflection of 420 mm as compared to a maximum midpoint deflection of 698 mm obtained experimentally, see Table 13.

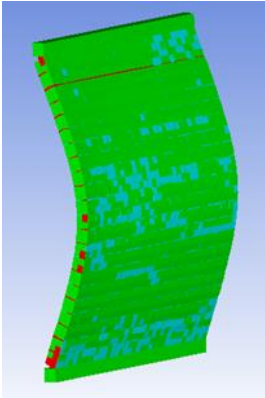
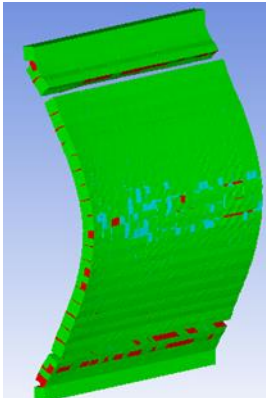


**Table 13: Deformation and failure shapes obtained numerically and experimentally for the case of CMU wall retrofitted with single layer PUNO (Wall #1)**

Beginning of the Failure	Final Stage	
		<p>Numerical Results obtained using AUTODYN hydrodynamic code</p>
		<p>Experimental results obtained using Blast Load Simulator (BLS)</p>

### 5.5.2 Wall #2 Results

Wall #2 is retrofitted with a single layer of PUNO that is 2 mm in thickness. The pressure of 172.4 kPa is applied to the wall using an impulse of 1144.5 kPa\* ms. Wall #2 failed at the end near the supports. The maximum midpoint deflection of 408 mm as compared to a maximum midpoint deflection of 457.2 mm obtained experimentally, see Table 14 .

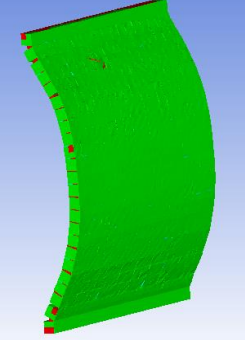
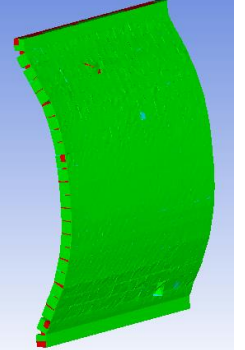
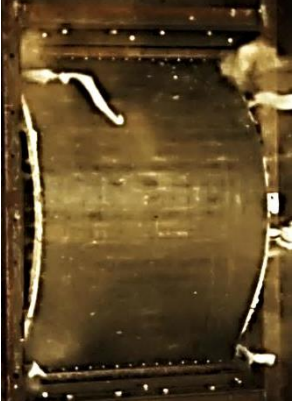

**Table 14: Deformation and failure shapes obtained numerically and experimentally for the case of CMU wall retrofitted with single layer PUNO (Wall #2)**

Beginning of the Failure	Final Stage	
		<p>Numerical Results obtained using AUTODYN hydrodynamic code</p>
		<p>Experimental results obtained using BLS</p>

### 5.5.3 Wall #3 Results

Wall #3 is retrofitted with a double layer system. The first layer is PUPM3PO that is 2 mm in thickness and the second layer is EG10APP10PO that is 1 mm in thickness. The pressure of 172.4 kPa is applied using an impulse of 1144.5 kPa\* ms. Wall #3 failed at the end near the supports experimentally due to a manufacturing error. The maximum midpoint deflection of 255 mm as compared to a maximum midpoint deflection of 495 mm obtained experimentally, see Table 15 .

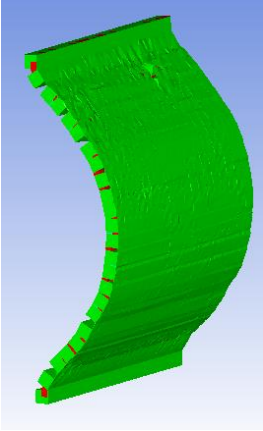
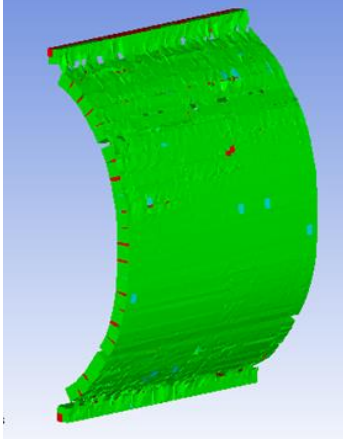


**Table 15: Deformation and failure shapes obtained numerically and experimentally for the case of CMU wall retrofitted with double layer PUPM3PO +EG10APP10PO (Wall #3)**

Beginning of the Failure	Final stage	
		<p>Numerical Results obtained using AUTODYN hydrodynamic code</p>
		<p>Experimental results obtained using BLS</p>

#### 5.5.4 Wall #4 Results

Wall #4 is retrofitted with a single layer of PUPM3PO that is 2 mm in thickness. The pressure of 172.4 kPa is applied using an impulse of 1144.5 kPa\* ms. Wall #4 failed at the end near the supports. The maximum midpoint deflection of 523.4 mm through the simulations, however there is not a comparison with the experiment, see Table 16 . This is due to the fact the Wall #4 did not withstand blast and came apart.

**Table 16: Deformation and failure shapes obtained numerically and experimentally for the case of CMU wall retrofitted with single layer PUPM3PO (Wall #4)**

Beginning of the Failure	Final stage	
		<p>Numerical Results obtained using AUTODYN hydrodynamic code</p>
		<p>Experimental results obtained using BLS</p>

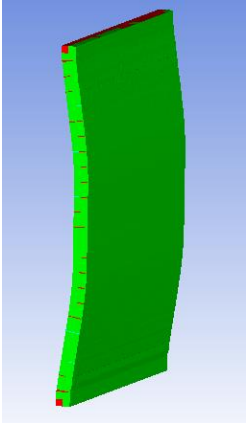
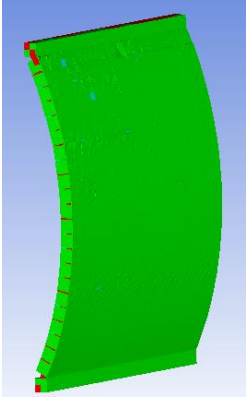


### 5.5.5 Wall #5 Results

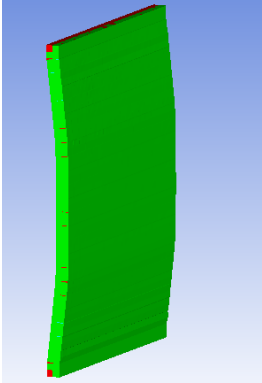
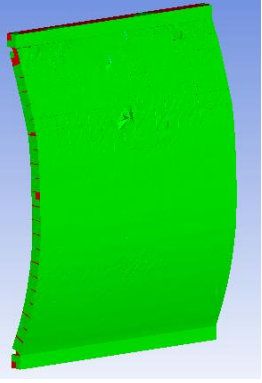
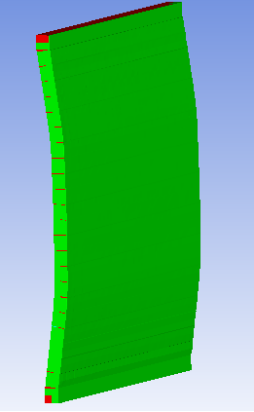
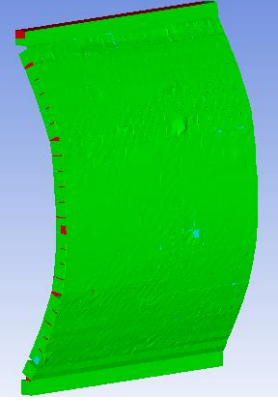
Wall #5 is retrofitted with a double layer system. The first layer is PUPM3PO that is 2 mm in thickness and the second layer is EG10APP10PO that is 1 mm in thickness. This is experimentally tested wall tested three times at pressures of 68.9kPa, 103.4 kPa, and 137.9 kPa. These results are compared to three individually run simulations and each pressure is applied using an impulse of 1144.5 kPa\* ms. The

maximum midpoint deflection for 68.9kPa of 258 mm as compared to a maximum midpoint deflection of 254 mm obtained experimentally.

Due to the limited supply of test specimens Wall #5 is tested again with 103.4 kPa and 137.9 kPa. Therefore, there are not accurate experimental results for the comparison. The maximum midpoint deflection for 103.4 kPa and 137.9 kPa is obtained computationally only. The maximum midpoint deflection at 103.4 kPa is 269.1 mm. The maximum midpoint deflection at 137.9 kPa is 278 mm. These results are given in Table 17 .

**Table 17: Deformation and failure shapes obtained numerically and experimentally for the case of CMU wall retrofitted with double layer PUPM3PO +EG10APP10PO (Wall #5)**

Pressure	Beginning of Deflection	Maximum Deflection	
68.9 kPa			Numerical Results obtained using AUTODYN hydrodynamic code
68.9 kPa			Experimental results obtained using BLS

103.4 kPa			Numerical Results obtained using AUTODYN hydrodynamic code
137.9 kPa			Numerical Results obtained using AUTODYN hydrodynamic code

**Table 18: Midpoint deflection**

Wall Number	Maximum Midpoint deflection (mm)	
	Experiments	Finite element
Wall #1	698	420
Wall #2	457.2	408
Wall #3	495	255
Wall #4	N.A.	523.4
Wall #5 (68.9kPa)	254	258
Wall #5 (103.4kPa)	N.A.	269.1
Wall #5 (137.9kPa)	N.A.	278



## 5.6 Parametric Evaluation

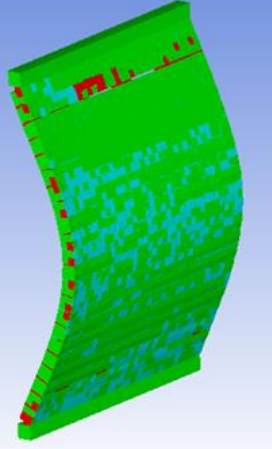
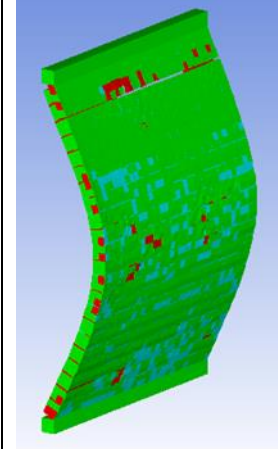
### 5.6.1 Adhesion

Following the comparison of results between the experimental and the computational model the decision is made to evaluate the effect of adhesion of the retrofit material with the CMU wall. This is done by repeating the computational tests with the same models and pressures, but joining the retrofit material with the CMU wall. By joining the retrofit material with the CMU wall perfect bonding between them can be simulated.

#### 5.6.1.1 Wall # 1

The maximum midpoint deflection of 420 mm as compared to a maximum midpoint deflection of 236 mm obtained when perfect bonding is assumed, see Table 19. This shows a 43.8% decrease in the maximum midpoint deflection when perfect bonding is assumed.

**Table 19: Maximum Midpoint Deflection between Models for Wall#1**

Beginning of the Failure	Final Stage	
		Numerical Results obtained using AUTODYN hydrodynamic code  Assuming no bonding with wall

		<p>Numerical Results obtained using AUTODYN hydrodynamic code</p> <p>Assuming perfect bonding with wall</p>
--	--	---

**5.6.1.2 Wall # 2**

The maximum midpoint deflection of 408 mm as compared to a maximum midpoint deflection 215.70 mm obtained when perfect bonding is assumed, see Table 20. There is a 47.13% decrease in the maximum midpoint deflection when perfect bonding is assumed.

**Table 20: Maximum Midpoint Deflection between Models for Wall#2**

Beginning of the Failure	Final Stage	
		<p>Numerical Results obtained using AUTODYN hydrodynamic code</p> <p>Assuming no bonding with wall</p>

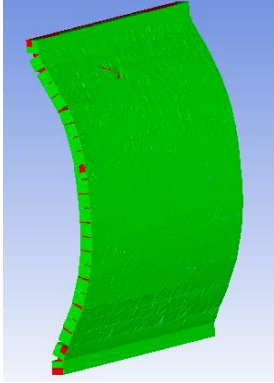
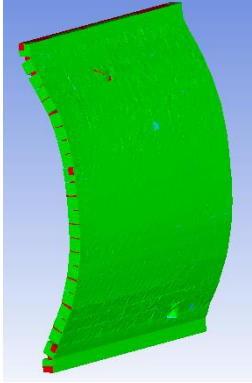
		<p>Numerical Results obtained using AUTODYN hydrodynamic code</p> <p>Assuming bonding with wall</p>
--	--	---

### 5.6.1.3 Wall # 3

The maximum midpoint deflection of 255 mm as compared to a maximum midpoint deflection of 211.5 mm obtained when perfect bonding is assumed, see Table 21. There is a 17.06% decrease in the maximum midpoint deflection when perfect bonding is assumed.

**Table 21: Maximum Midpoint Deflection between Models for Wall#3**

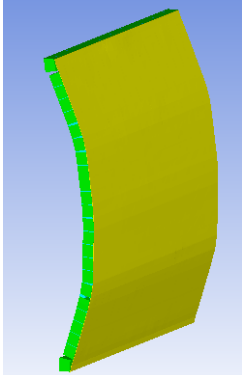
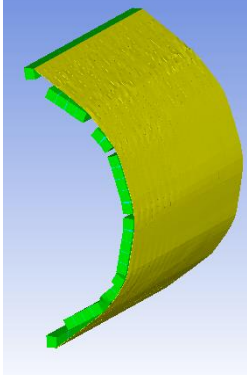
Beginning of the Deflection	Final stage	
		<p>Numerical Results obtained using AUTODYN hydrodynamic code</p> <p>Assuming no bonding with wall</p>

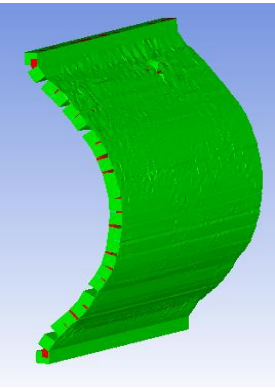
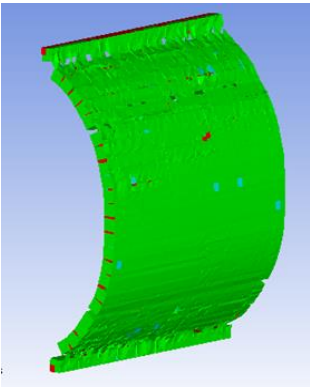
		<p>Numerical Results obtained using AUTODYN hydrodynamic code</p> <p>Assuming bonding with wall</p>
---	---	---

#### 5.6.1.4 Wall #4

The maximum midpoint deflection of 523.4 mm as compared to 373.3 mm obtained when perfect bonding is assumed, see Table 22. There is a 28.68 % decrease in the maximum deflection when perfect bonding is assumed.

**Table 22: Maximum Midpoint Deflection between Models for Wall#4**

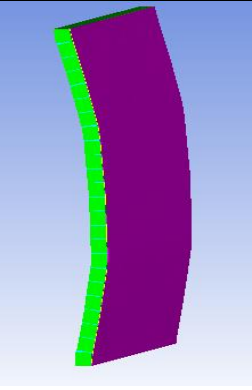
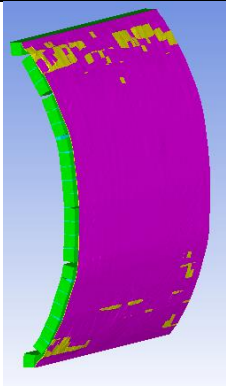
Beginning of the Failure	Final stage	
		<p>Numerical Results obtained using AUTODYN hydrodynamic code</p> <p>Assuming no bonding with wall</p>

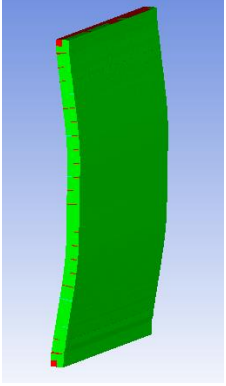
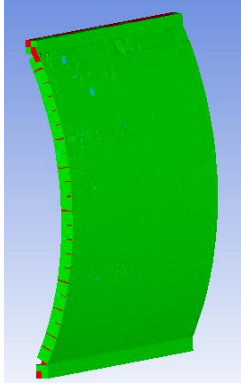
		<p>Numerical Results obtained using AUTODYN hydrodynamic code</p> <p>Assuming bonding with wall</p>
---	---	---

### 5.6.1.5 Wall #5

The maximum midpoint deflection for 68.9kPa of 258 mm as compared to a maximum midpoint deflection of 162.3 mm obtained when perfect bonding is assumed, see Table 23. There is a 36.10 % decrease in the maximum midpoint deflection when perfect bonding is assumed.

**Table 23: Maximum Midpoint Deflection between Models for Wall#5**

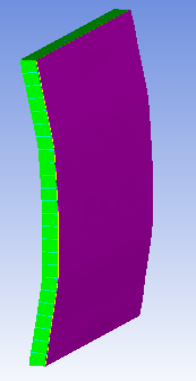
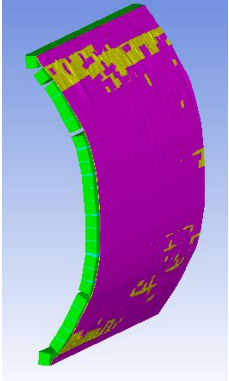
Pressure	Beginning of Deflection	Maximum Deflection	
68.9 kPa			<p>Numerical Results obtained using AUTODYN hydrodynamic code</p> <p>Assuming no bonding with wall</p>

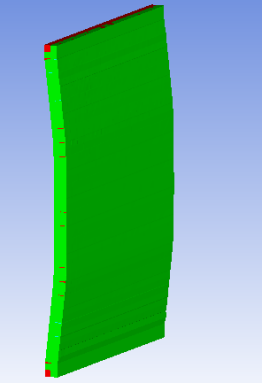
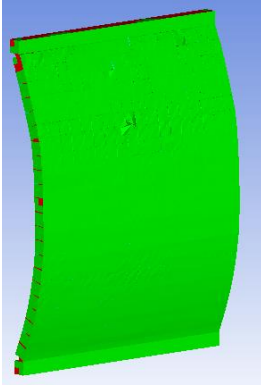
68.9 kPa			<p>Numerical Results obtained using AUTODYN hydrodynamic code</p> <p>Assuming bonding with wall</p>
----------	---	--	---

**5.6.1.6 Wall # 6**

The maximum midpoint deflection of 269.1 mm as compared to a maximum midpoint deflection of 170.7 mm obtained when perfect bonding is assumed, see Table 24. There is a 39.04% decrease in the maximum midpoint deflection when perfect bonding is assumed.

**Table 24: Maximum Midpoint Deflection between Models for Wall#6**

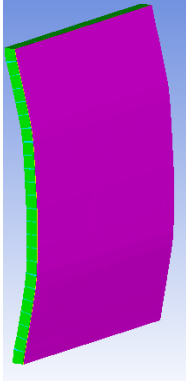
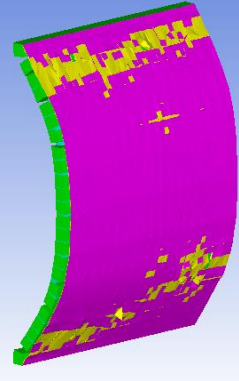
Pressure	Beginning of Deflection	Maximum Deflection	
103.4 kPa			<p>Numerical Results obtained using AUTODYN hydrodynamic code.</p> <p>Assuming no bonding with wall</p>

103.4 kPa			<p>Numerical Results  obtained using  <b>AUTODYN</b>  hydrodynamic code  Assuming bonding  with wall</p>
-----------	---	--	--

### 5.6.1.7 Wall #7

The maximum midpoint deflection is found to be 278 mm without bonding to the wall and 217.9 mm with bonding to the wall, see Table 25. There is a 21.61% decrease in the maximum midpoint deflection when perfect bonding is assumed.

**Table 25: Maximum Midpoint Deflection between Models for Wall#7**

Pressure	Beginning of Deflection	Maximum Deflection	
137.9 kPa			<p>Numerical Results  obtained using  <b>AUTODYN</b>  hydrodynamic code  Assuming no  bonding with wall</p>

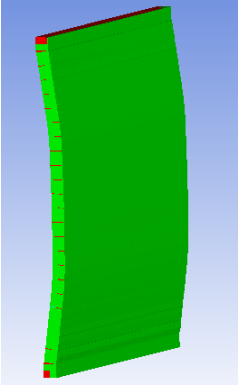
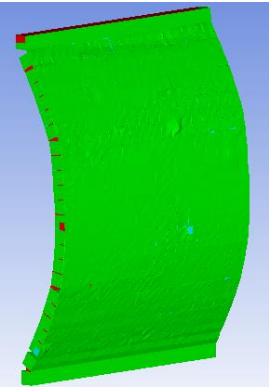
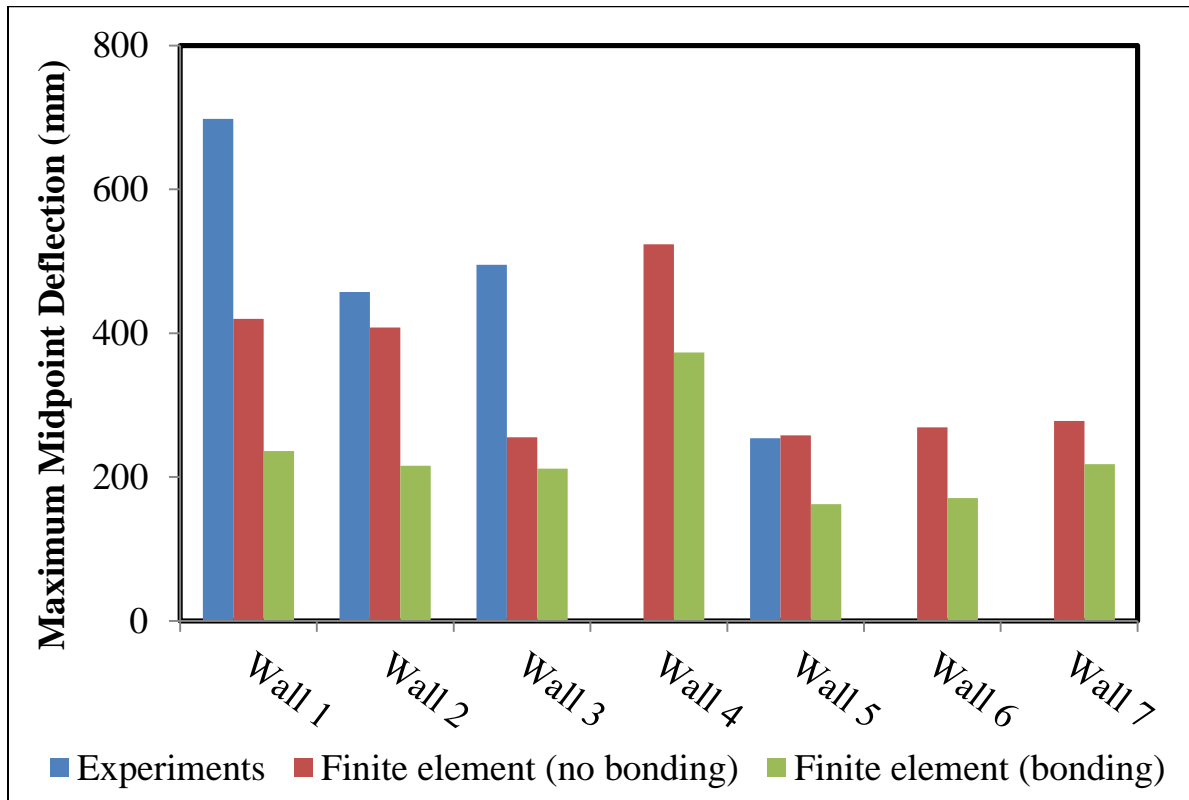
<p>137.9 kPa</p>			<p>Numerical Results obtained using AUTODYN hydrodynamic code Assuming bonding with wall</p>
----------------------	---	--	--

Table 26 shows a comparison of the maximum midpoint deflection between the experimental results, and the bonded and non-bonded computational results. From the table it can be seen the finite element results are generally lower than the experimental results. This is mainly due to the simulated environment being idealized rather than the realistic setting of the experiment. Also, the finite element results that assumed no bonding with the CMU wall were closer to the experimental results than those that assumed perfect bonding. That potentially indicates a future need to study the bonding and adhesion of the CMU wall and retrofit materials. Figure 30 gives a visual representation of the maximum midpoint deflection results. In this figure it can be seen that the double layer system of PUPM3EG10APP10 appears to perform better in experimental, and both computational results in terms of having the lowest maximum midpoint deflection.



**Table 26: Midpoint Deflection Comparison of Bonding**

Wall Number	Maximum Midpoint deflection (mm)		
	Experiments	Finite element (no bonding)	Finite element (bonding)
Wall #1	698	420	236
Wall #2	457.2	408	215.7
Wall #3	495	255	211.5
Wall #4	N.A.	523.4	373.3
Wall #5 (68.9kPa)	254	258	162.3
Wall #5 (103.4kPa)	N.A.	269.1	170.7
Wall #5 (137.9kPa)	N.A.	278	217.9



**Figure 30: Midpoint deflection represented in a bar chart for the experimental vs. simulation (no bonding, bonding)**

## 5.6.2 Full Scale Validation

After simulating the  $\frac{1}{4}$ <sup>th</sup> scale experimental CMU walls, simulations are needed to validate the full scale applications of the retrofit materials. To be consistent the same material model mentioned previously are still utilized for these models. The full scale CMU wall is 14 blocks in height and 9 blocks in width. The wall geometry and finite element for the simulation setup are shown in Figure 31. These simulations are done assuming perfect bonding between the material coating and the CMU wall. The initial simulations are done using the exact pressure and impulse utilized in the  $\frac{1}{4}$ <sup>th</sup> scale simulations, which did not produce usable results. Then, from the literature it is determined that specific parameters must be scaled, see Table 27 (Irshidat 2011). From Table 27 it is determined that the time for the applied impulse and material reference strain rate must be scaled. For this case a scale factor of 3 is used, the scaling includes the 2 mm coating thickness which is scaled to 6 mm.

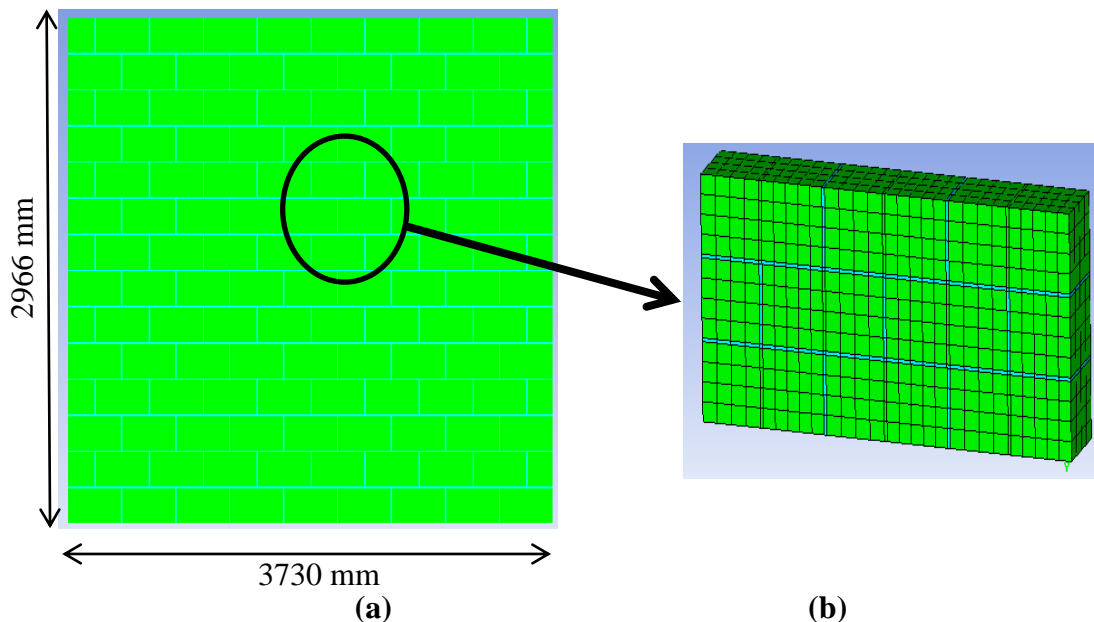


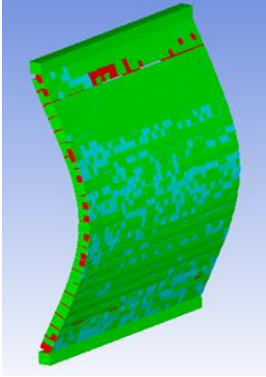
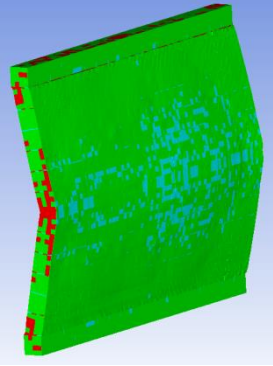
**Figure 31: Full Scale Wall: (a) Geometry (b) F. E. Mesh**

**Table 27: Stress-Inertia Scaling (Irshidat et al. 2011)**

Parameter	Dimension	Scale factor
Length	$L$	$SF$
Time	$T$	$SF$
Force	$F$	$SF^2$
Velocity	$LT^{-1}$	$SF^0$
Acceleration	$LT^{-2}$	$SF^{-1}$
Density	$FL^{-4}T^2$	$SF^0$
Mass	$FL^{-1}T^2$	$SF^3$
Pressure	$FL^{-2}$	$SF^0$
Stress	$FL^{-2}$	$SF^0$
Energy	$FL$	$SF^3$
Strain		$SF^0$
Strain rate	$T^{-1}$	$SF^{-1}$

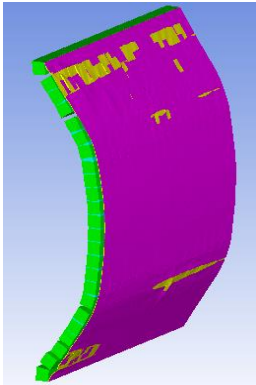
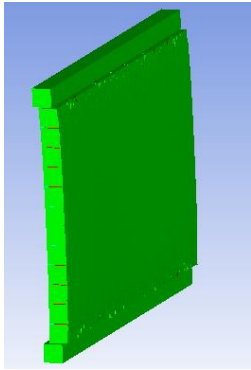
For the PUNO full scale simulations the applied pressure is 206.8 kPa and the impulse is 3430.8 kPa\*ms. The results show a maximum midpoint deflection of 306.2 mm. This is a 29.66% increase from the 236 mm maximum midpoint deflection that is shown on the perfectly bonded  $\frac{1}{4}$ <sup>th</sup> scale model. This comparison is shown in Table 28.

**Table 28:  $\frac{1}{4}$ <sup>th</sup> scale vs. Full scale for PUNO Coating**

$\frac{1}{4}$ <sup>th</sup> Scale Maximum Midpoint Deflection	Full Scale Maximum Midpoint Deflection	
		Numerical Results obtained using AUTODYN hydrodynamic code  Assuming bonding with wall

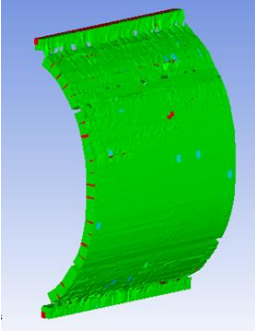
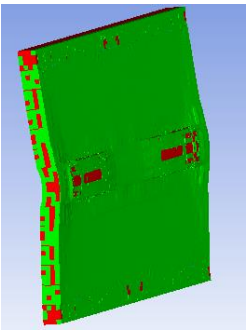
For the double layer system of PUPM3PO +EG10APP10PO full scale simulation the applied pressure is 172.4 kPa and the impulse is 3430.8 kPa\*ms. The results show a maximum midpoint deflection of 100 mm. This is a 52.6% decrease from 211 mm maximum midpoint deflection that is shown on the perfectly bonded 1/4<sup>th</sup> scale model, shown in Table 29.

**Table 29: 1/4<sup>th</sup> scale vs. Full scale for PUPM3PO+EG10APP10PO Coating**

1/4 <sup>th</sup> Scale Maximum Midpoint Deflection	Full Scale Maximum Midpoint Deflection	
		<p>Numerical Results obtained using AUTODYN hydrodynamic code</p> <p>Assuming bonding with wall</p>

For the PUPM3PO full scale simulation the applied pressure is 172.4 kPa and the impulse is 3430.8 kPa\*ms. The results show a maximum midpoint deflection of 152 mm. This is a 52.6% decrease from the 373 mm maximum midpoint deflection shown on the perfectly bonded 1/4<sup>th</sup> scale model, shown in Table 30.

**Table 30: 1/4<sup>th</sup> scale vs. Full scale for PUPM3PO Coating**

1/4 <sup>th</sup> Scale Maximum Midpoint Deflection	Full Scale Maximum Midpoint Deflection	
		<p>Numerical Results obtained using AUTODYN hydrodynamic code</p> <p>Assuming bonding with wall</p>

There are several potential causes of these large percent differences between the 1/4<sup>th</sup> scale models and the full scale models. It may be a product of improperly scaled boundary conditions. The mesh size may not be fine enough to produce accurate results. Overall, the validation of utilizing 1/4<sup>th</sup> scale models and translating them into full scale application requires much further investigation.

### 5.6.3 Thickness Evaluation

The P-I curves define the limiting values for each thickness and at set pressure and impulse, as well as, the damage produced in the structural component (Shi et al. 2008). To develop the P-I curves a multitude of simulations have to be performed using the finite element software ANSYS AUTODYN.

Simulations at set up for using 1/4<sup>th</sup> scale CMU wall for with the PUNO, PUPM3PO+EG10APP10PO, and PUPM3PO coating materials each beginning

with a 2 mm thickness. These tests are run at set pressures and the impulses are varied until the point of failure is determined. This process is then repeated for different pressures at various impulses which are then used to develop the P-I curves. The data points for 2 mm thick retrofit layer for each material are plotted as P-I curves in Figure 32, Figure 33, and Figure 34 . To provide smoother curves many more simulations would need to be performed at more pressures provide more data points. This is a very time consuming process that takes anywhere from 10 to 20 simulations to ascertain each individual data point. Future work will be required to generate a full set of P-I curves for various material coating thicknesses.

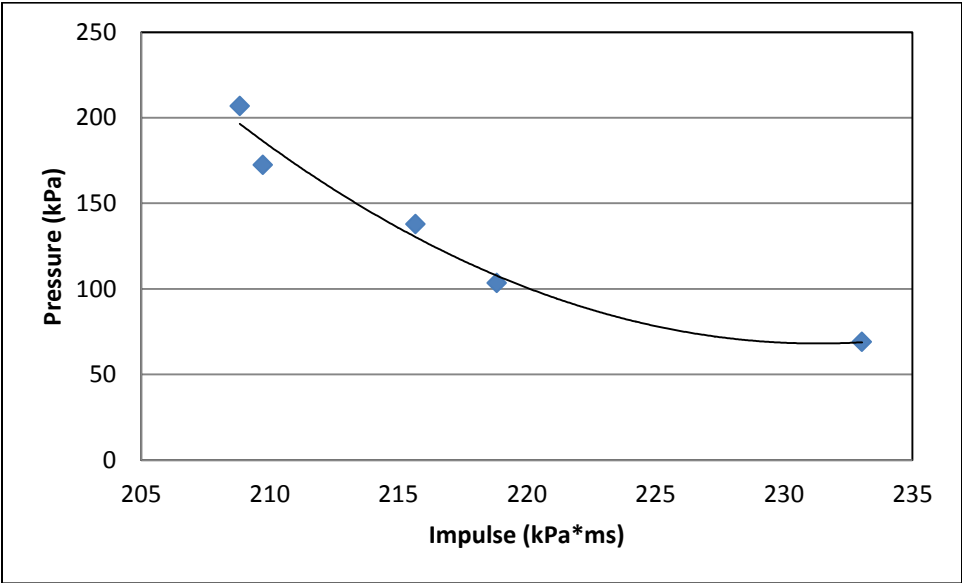


**Figure 32: P-I Curve for PUNO**

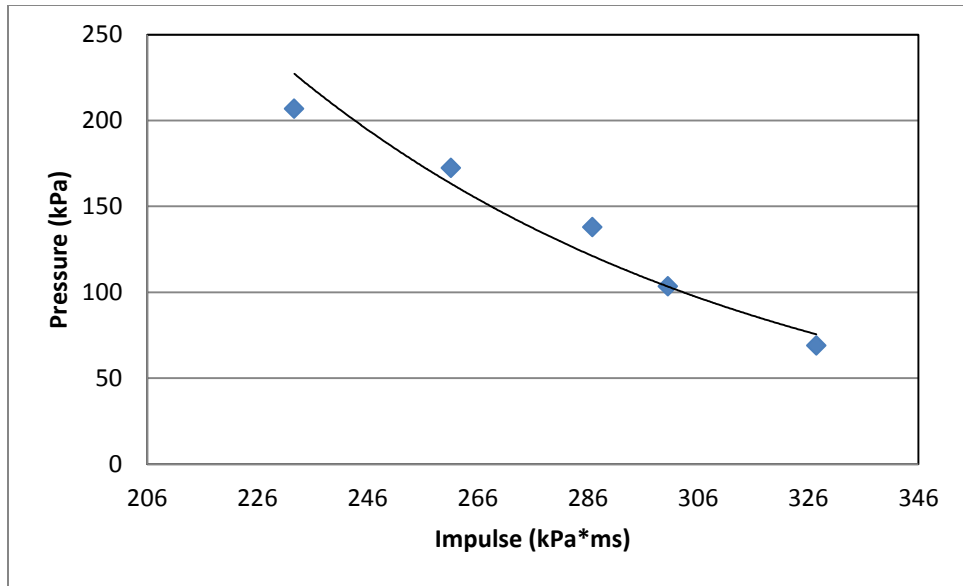


**Figure 33: P-I Curve for PUPM3PO+EG10APP10PO**

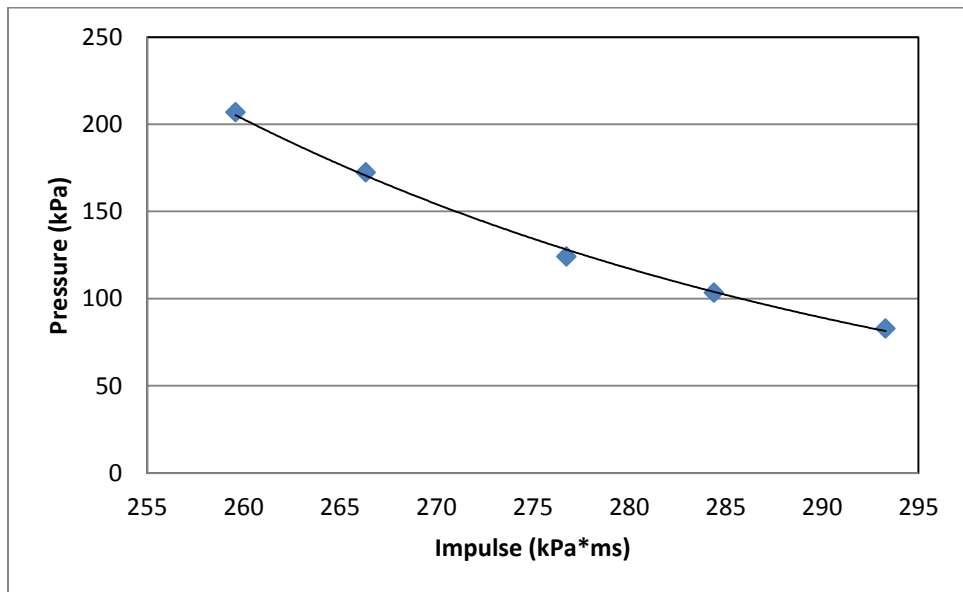


**Figure 34: P-I Curve for PUPM3PO**

#### 5.6.4 Single Degree of Freedom

Single degree of freedom systems are commonly used to measure the dynamic response of a structural system. This ¼<sup>th</sup> scale CMU system is reduced to a single degree of freedom (SDOF) system that is simply supported. The blast loading is reduced to a rectangular, uniformly distributed pressure, see Figure 35. The focus is on the equation of motion, Equation 5, used to determine maximum displacement at the midpoint of the concrete masonry unit wall subjected to various loads. The parameters for this equation include mass ( $m$ ), a damping coefficient ( $c$ ), and a stiffness coefficient ( $k$ ).

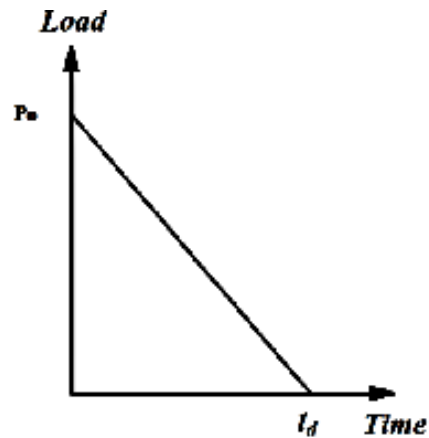


**Figure 35: Triangular Load Approximation (Irshidat 2010)**

$$m\ddot{y} + c\dot{y} + ky = P(t)$$

#### **Equation 5: Equation of Motion**

The parameters for this system are then determined by transformation factors that convert the real world system to an equivalent system. These transformation



factors are based on simplified structure of the system. The transformation factors are given in Table 31.

**Table 31: Transformation Factors (Biggs 1964)**

	<b>Transformation Factors</b>		
	<b>Load Factor (<math>K_L</math>)</b>	<b>Mass Factor (<math>K_M</math>)</b>	<b>Load-Mass Factor (<math>K_{LM}</math>)</b>
<b>Plastic Region</b>	0.50	0.33	0.66
<b>Elastic Region</b>	0.64	0.50	0.78

The equivalent mass used for this system is determined by averaging the load-mass factor between the elastic and plastic regions and then multiplying it by the total mass of the system. The total mass of the system was calculated by using the density of the masonry wall and its area and the density of the retrofit material and its area.

The damping of this system was considered to be negligible. The consideration was determined due to the fact that it is not a major contributor in maximum deflection for blast loaded systems this reduces the equation as seen in Equation 6.

$$m\ddot{y} + ky = P(t)$$

**Equation 6: Reduced Equation of Motion**

The load-deflection curves or resistance function for composite materials can then be determined using finite element software, such as ANSYS or SAP2000.

For non-hyper elastic materials, such as a commercial polyurea from Protective coating Inc., see Figure 36, these resistance functions can be fitted with an equivalent bilinear line using an energy-based method (Irshidat et al. 2011). From the equivalent bilinear line two things are determined. First, the stiffness coefficients are calculated from the slopes of the equivalent bilinear lines, see Figure 37 . Second, the yield point of the material is obtained as it is the point that separates the lines from one another.

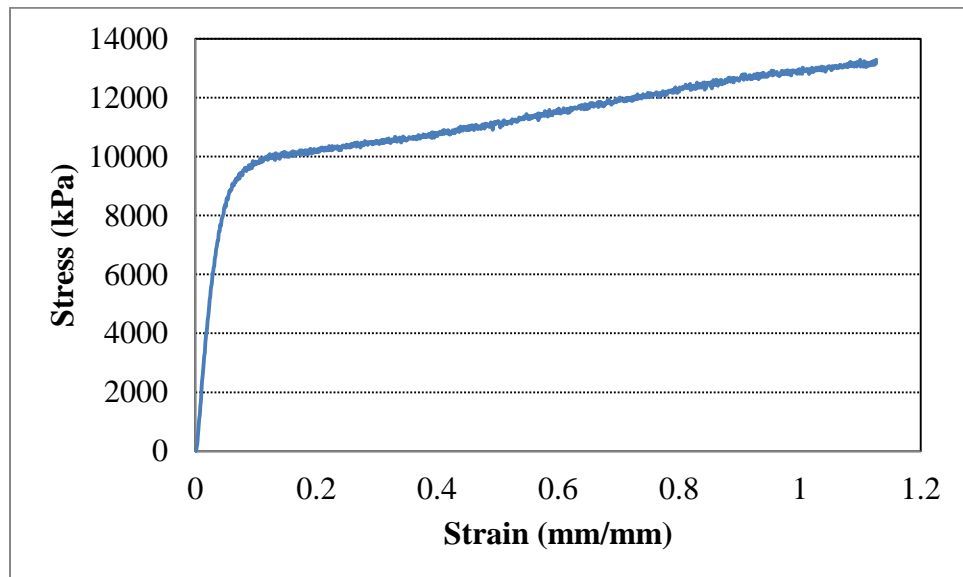


**Figure 36: Stress-Strain Curve for a commercial Polyurea (Irshidat 2010)**

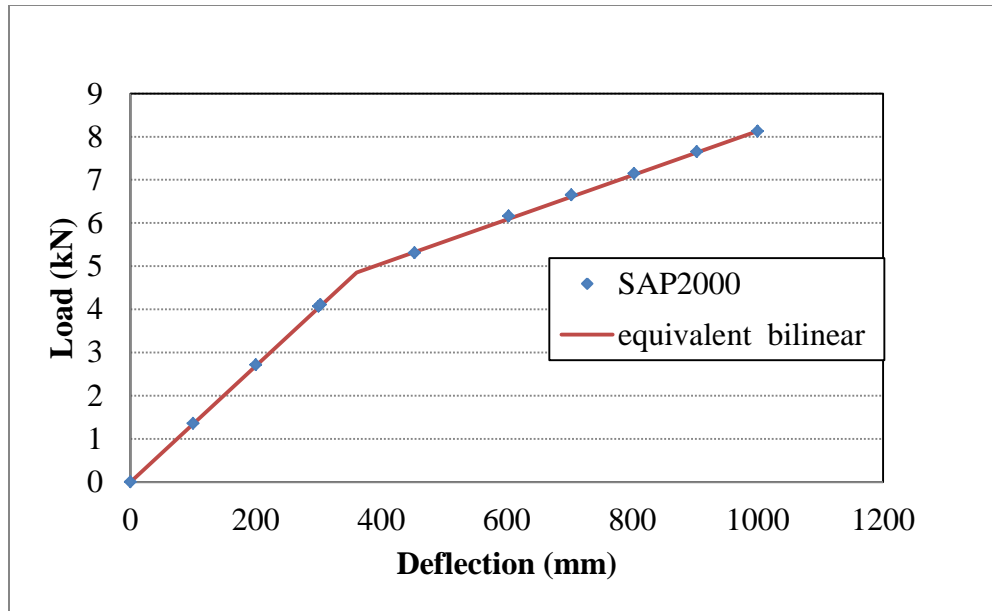


**Figure 37: Resistance Function for a Pure Polyurea (Irshidat 2010)**

However, the polyurea utilized in this research is hyper-elastic, see Figure 38. The resistance function for this material is determined using ANSYS. However, due to the hyper-elastic nature the resistance function for this coating is found to be a linear line as shown in Figure 39. It is probable that the yield point of this is not uniquely identifiable because the deviation from linearity is very gradual. Further investigation into the determination of the resistance functions for hyper-elastic materials will be required to effectively complete the single degree of freedom model for this system. This is also, the case for PUPM3PO single layer and PUPM3PO+EG10APP10PO double layer systems. These materials are both hyper-elastic, as shown in Figure 40 and Figure 41. Due to their hyper-elasticity they too produce linear lines as resistance functions, as shown in Figure 42 and Figure 43.

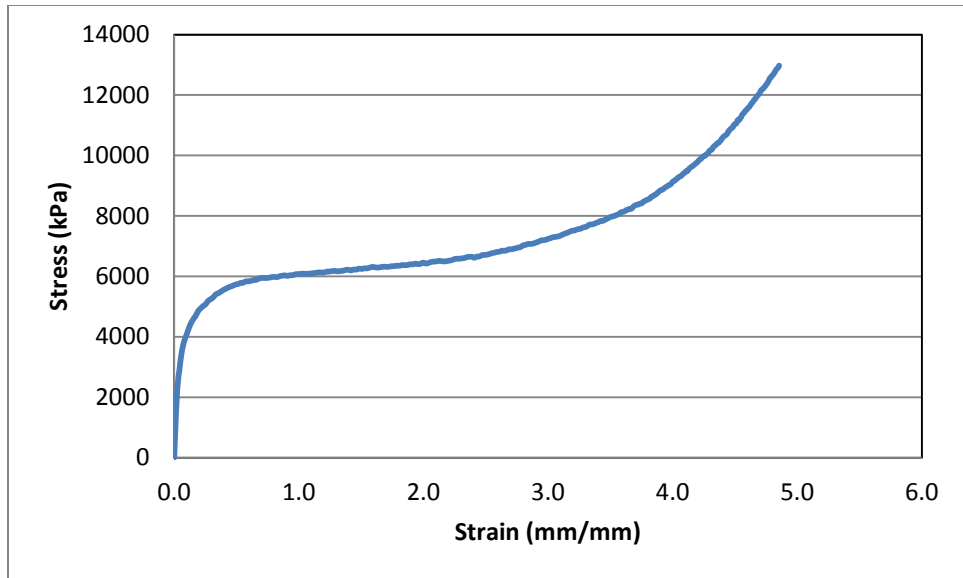


**Figure 38: Stress-Strain Curve for PUNO**

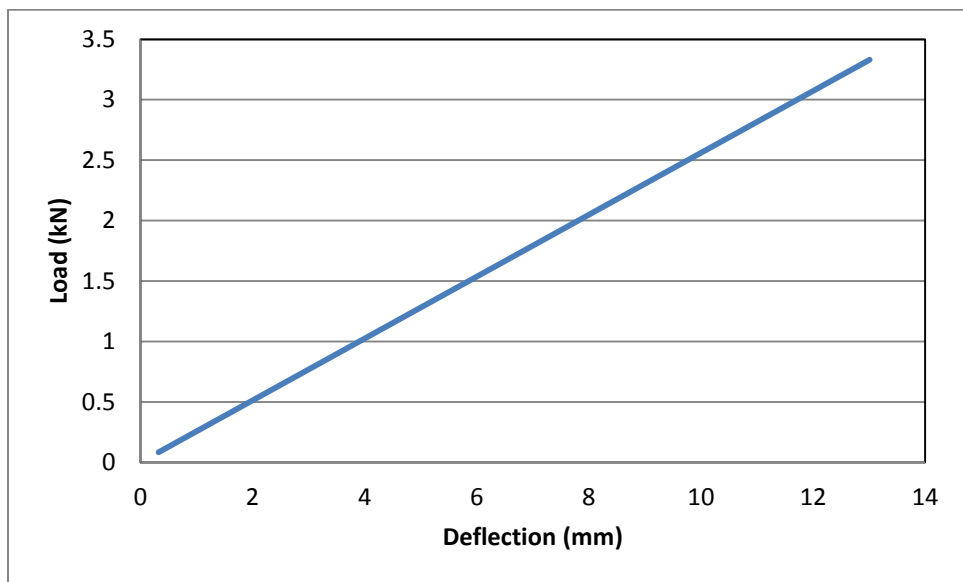


**Figure 39: Resistance Function for PUNO**

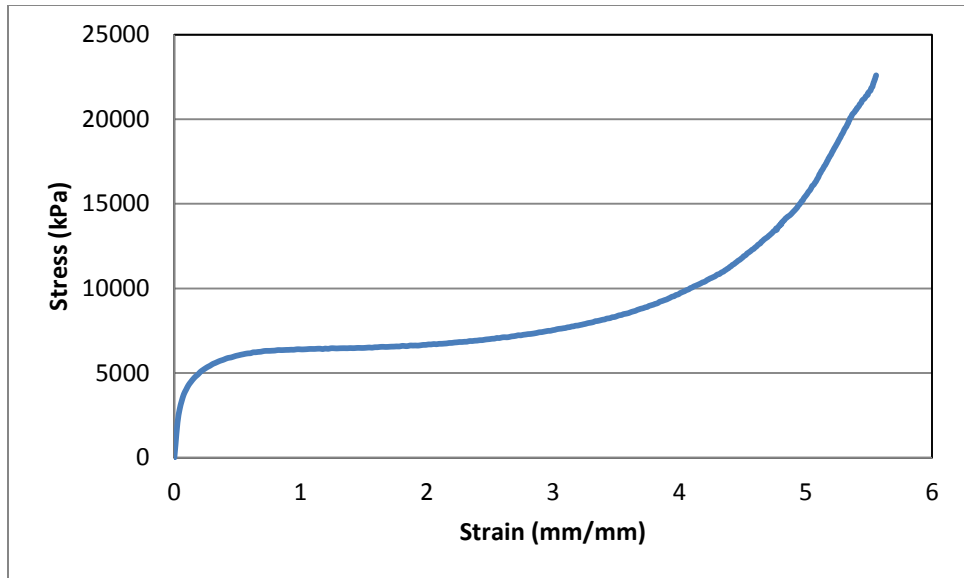


**Figure 40: Stress-Strain Curve for PUPM3PO**

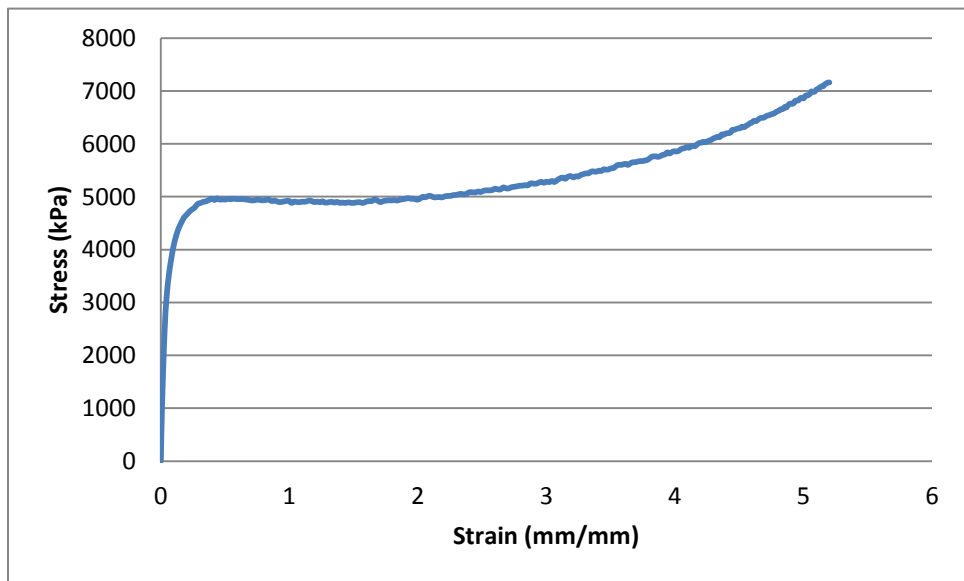


**Figure 41: Stress-Strain Curve for EG10APP10PO**

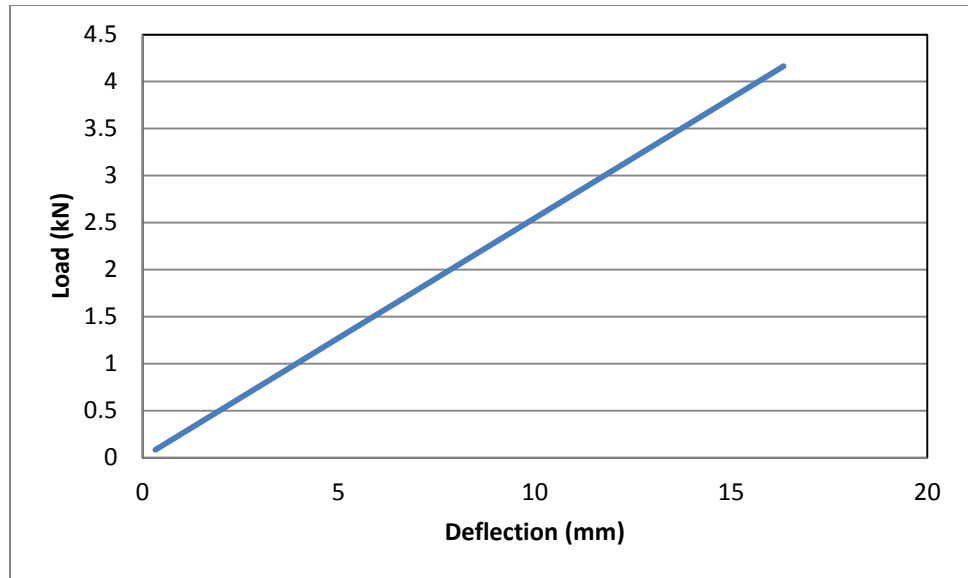


**Figure 42: Resistance Function for PUPM3PO**

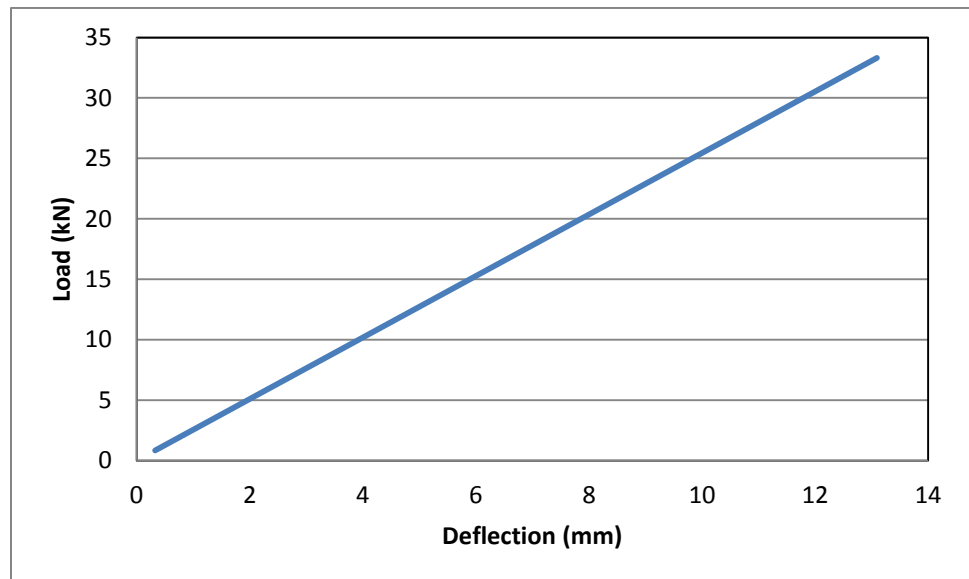


**Figure 43: Resistance Function for PUPM3PO+EG10APP10PO**

## VI. CONCLUSION

### DMA

- Nineteen nanocomposite materials are tested on the DMA Q800 series using frequency sweeps to ascertain their strain rate sensitivities.
- The best performing materials for each class of nanocomposites is determined. These materials include: PUCS10PO, PUFA20PO, PUNC3PO, PUPM1PO, and PUEG40APP40PO.
- The PUPM1PO actually appears to show more improved dynamic properties than the PUPM3PO that is selected from testing. However, PUPM3PO has been selected to pursue further evaluation and testing due to its fire performance
- The PUEG40APP40PO shows better dynamic properties compared to PUEG10APP10PO, the latter is selected for its workability and fire performance.

### Material Multi-Functionality

- To further optimize the material coating selected for blast testing material multi-functionality is utilized.
- Several multi-functionality parameters have been considered, such as PHRR, tensile strength, and energy at breakage.
- Fire testing is performed using a cone calorimeter to measure the heat release rate of all the nanoenhanced coating materials, and the PHRR as well

- The lower the PHRR is the more fire retardant capabilities the material possesses.
- Uni-axial tension tests are performed using the Instron machine, from these tests the tensile strength of the material and energy at the material's breaking point are determined.
- The best performing materials in terms of their multi-functionality are: PUPM3PO, PUEG10APP10PO, and PUEG40APP40PO.
- From these materials only PUPM3PO and PUEG10APP10PO are used for blast testing.
- PUPM0.5PO is not used for blast testing due to the dripping it showed during the fire testing, which makes it an ineffective fire retardant material. PUEG40APP40PO is not used for blast testing because it has a high viscosity which gives it a low workability, and a very short setting time. This material will be difficult to translate into practical application.

#### Experimental/Numerical Results

- The experimental results for Wall #5, which is the double layer system of PUPM3PO + EG10APP10PO, shows the smallest maximum midpoint deflection which is 254 mm. With the applied pressure of 68.9 kPa.
- In finite element simulation, however, the smallest midpoint deflection is found in Wall #3. This is also a double layer system of PUPM3PO + EG10APP10PO, however the applied pressure is 172.4 kPa.



- The finite element results compared with the experiment are performed assuming no bonding to the CMU wall. It is considered to necessary to test the effects of adhesion of the coating material with the CMU wall. Further, all simulations are performed again, this time assuming a perfect bond with the CMU wall. For all cases there is a significant reduction in the maximum midpoint deflection of the CMU wall when perfect bonding is assumed.

### Full Scale Validation

- Full scale validation requires the stress-inertia scaling be applied to the time and strain rate variables as well as the dimensions in order to properly function.
- There are significant differences in the maximum midpoint deflection values obtained from the full scale models when compared to the  $\frac{1}{4}$ <sup>th</sup> scale models.
- These differences may be caused by a mesh size that is too crude or short time cycles.

### Single Degree of Freedom

- Ideally a resistance function needs to be determined to locate a yield point.
- Due to the hyper-elastic nature of the materials used (i.e. PUNO) the resistance functions create only linear lines.
- This may be because the yield point occurs at small strain values compared to strain at breakage; hence, it is to accurately determine it from typical stress-strain curves of hyper-elastic polymers.

- Further investigation into the determination of a resistance function for these materials is required to complete a single degree of freedom model.

#### Thickness Evaluation

- Each material coating system is evaluated at several pressures with varying impulses to determine the point of failure for several thicknesses.
- This allows for the creation of a Pressure-Impulse curve to evaluate the performance of the selected material for similar blast events.
- To provide a smoother curve for each material coating more pressures should be evaluated.
- Future work for this evaluation includes determining P-I curves for various thicknesses of the coating material, thus allowing the industry a tool to use in which the appropriate material coating and thickness for their desired needs can be ascertained.

#### Future Work

- Investigate the effects of hyper-elasticity on resistance functions.
- Complete single degree of freedom model for these material coating systems.
- More complete Full Scale validation.
- Create a more complete thickness evaluation to provide a more comprehensive P-I diagram for the material coating systems.

## REFERENCES

- Biggs, J. M. *Introduction to Structural Dynamics*. New York: McGraw-Hill, 1964.
- Centrury Dynamics, Inc. *AUTODYN Theory Manual, Revision 10.0*. Concord, CA: Centrury Dynamics, Inc., 2006.
- Davidson, James S., et al. "Failure Mechanisms of Polymer-Reinforced Concrete Masonry Walls Subjected to Blast." *Journal of Structural Engineering* 131 (2005): 1194-1205.
- "Dynamic Mechanical Analysis (DMA)." *Theory and Applications*. TA Instruments, 2006.
- Ibeh, Christopher C. , et al. "Research and Education at the Center for Nanocomposites and Multifunctional Materials [CNCMM], Pittsbury State University." *2007 ASEE Midwest Section Conference: Teaching Methods III*. Wichita: American Society for Engineering Education, 2007.
- Irshidat, M., et al. "Nanoparticle Reinforced Polymer for Blast Protection of Unreinforced Masonry Wall: Laboratory Blast Load Simulation and Design Models." *Journal of Structural Engineering* 137 (2011): 1193-1204.
- Irshidat, Mohammed. "Physics-based Simulation and Experiment on Blast Protection of Infill Walls and Sandwich Composites Using New Generation of Nano Particle Reinforced Materials." The University of Mississippi, 2010.
- Kessler, M.R., N.R. Sottos and S.R. White. "Self-Healing Structural Composite Materials." *Composites Part A: Applied Science and Manufacturing* (2003): 743-753.
- MacAloney, Neil, et al. *Viscoelastic Characterization of Aliphatic Polyurethane Interlayers*. Aberdeen Proving Ground: Army Research Laboratory, 2007.
- Maji, Arup K., Jay P. Brown and Gorum S. Urgessa. "Full-Scale Testing and Analysis for Blast-Resistant Design." *Journal of Aerospace Engineering* 21 (2008): 217-225.
- Oesterle, Michael G., Gilbert A. Hegemier and Kenneth B. Morrill. "Response of Concrete Masonry Walls to Simulated Blast Loads." *Don't Mess with Structural Engineers*. Structural Engineering Institute of ASCE, 2009. 1277-1286.
- Oliver, W. C. and G. M. Pharr. "Measurement of Hardness and Elastic Modulus by Instrumented Indentation: Advance in Understanding Refinements to Methodology." *Journal of Material Research* 19 (2004): 3-20.
- Raman, S. N., T. Ngo and P. Mendis. "A Review on the use of Polymeric Coating for Retrofitting of Structural Elements against Blast Effects." *Electronic Journal of Structural Engineering* 11 (2011): 69-79.

Razaqpur, A. Ghani, Ettore Contestabile and Ahmed Tolba. "Experimental study of the Strength and deformation of Carbon Fibre Reinforced Polymer (CFRP) Concrete Slabs under Blast Loads." *Canadian Journal of Civil Engineering* 36 (2009): 1366-1377.

Shi, Yanchao, Hong Hao and Zhong-Xian Li. "Numerical Derivation of Pressure-Impulse Diagrams for Prediction of RC Column Damage to Blast Loads." *International Journal of Impact Engineering* 35 (2008): 1213-1227.

"Thermal Analysis." TA Instruments, 2010.

Wei, Xueying and Mark G. Stewart. "Model Validation and Parameteric Study on the Blast Response of Unreinforced Brick Masonry Walls." *International Journal of Engineers* 37 (2010): 1150-1159.

Yi, J., et al. "Large Deformation Rate-Dependent Stress-Strain Behavior of Polyurea and Polyurethanes." *Polymer* 47 (2006): 319-329.

**APPENDIX**  
Fire Testing Experimental and Numerical

## **PROCEDURE**

### **MATERIALS**

Two types of materials are investigated in this paper: The first type comprises of experimental blast-resistant polymers based on an elastomer polymer (polyurea) or a thermoset polymer (epoxy). These polymers are reinforced with nanoadditives including exfoliated graphene nanoplatelets and polyhedral oligomeric silsesquioxane (POSS). POSS is a class of silicon-based nano chemicals designed to fulfill various mechanical functions supplied by Hybrid Plastics Inc., Hattiesburg, MS, USA.

Graphene nanoplatelets are typically less than 5 nm thick and can be synthesized with lateral dimensions ranging from less than 1  $\mu\text{m}$  to up to 100  $\mu\text{m}$ . Exfoliated graphene nanoplatelets-15 is made from Asbury 3772 (Asbury Carbons Inc., Asbury, NJ, USA) using high power microwave. Prior to the addition to epoxy resin, exfoliated graphene nanoplatelets are kitchen-microwaved for 1 min/10-15g. The second type of material is comprised of commercial fire resistant formulations. A detailed description for the fabricated material is summarized in the following sections:

#### **i. BLAST-RESISTANT MATERIALS**

Polyurea, LINE-X XS-350, is made of two prepolymers supplied by Protective Coating Inc., Kent, WA, USA. The polyurea is mixed with Polyhedral Oligomeric Silsesquioxane (POSS). Additionally, polyuria is mixed with exfoliated graphene platelets. Flexible epoxy is made of 100 phr (per hundred resin) Epon 828, 50 phr

Jeffamine D-400 and 25 phr Jeffamine D-2000. The polyurea and the epoxy blended with exfoliated graphene nanoplatelets are produced at Composite Materials & Structures Center, Michigan State University, East Lansing, MI, USA.

## ii. FIRE-RETARDANT MATERIALS

Four fire retardant materials are studied in this paper Tyfo<sup>®</sup> (LR), Tyfo<sup>®</sup> FC/F (LRFCF), Tyfo<sup>®</sup> HP (LRHP), and Tyfo<sup>®</sup> BLAST-Flex Type 4 (Type 4), supplied from Fyfe Inc., San Diego, CA, USA.

Tyfo<sup>®</sup>, LR, is a liquid rubber coating material (ethylene propylene rubber). Tyfo<sup>®</sup> FC/F is a two-part heat-resistant system applied in combination with Tyfo<sup>®</sup>. Tyfo<sup>®</sup> FC is a two-component fire resistant epoxy coating formulated to provide an increase in the existing fire rating. Tyfo<sup>®</sup> F is a one component formulation designed to be applied over Tyfo<sup>®</sup> FC. The Tyfo FC/F System will provide an increase to the fire rating of an element as per ASTM E-119 (2- hours wall rating) and provide a Class 1, ASTM E-84 flame and smoke rating. Tyfo<sup>®</sup> HP, LR HP, is a two-component epoxy fire retardant-intumescent coating based on non-halogenated phosphates. Tyfo<sup>®</sup> Blast-Flex Type 4, is two-component polyurea based systems with fire-resistance additive from Fyfe Inc.

## **EXAMINATION OF FIRE STATE**

### i. EXPERIMENTAL MEASUREMENTS (CONE CALORIMETER)



Cone calorimeter HRR measurements are made on a number of blast-resistant and fire-retardant coating materials on a FTT dual cone calorimeter. The samples are exposed to incident heat fluxes of 30, 40, 50 kW/m<sup>2</sup> with an exhaust flow of 24 L/s using the standardized test procedure (ASTM E-1354-07) with some modifications as described below.

All samples are tested without frame and grid, but the solid coating samples (polyurea, epoxy, and LR on cinder block) are tested in a shallow thick-walled aluminum dish to capture any dripping. The coated cinder block samples are wrapped with aluminum foil on the back side of the sample only to form a small pan that would capture any dripping off the sample surface during burning. The aluminum foil is not wrapped snugly around the sample so that any dripping behavior could be clearly observed.

## ii. NUMERICAL SIMULATIONS (FIRE DYNAMIC SIMULATOR)

Heat release rate (HRR) is an important property of materials that determines whether there is sufficient thermal energy for fire growth and spread. In addition to HRR, several other reaction properties are used to characterize the fire behavior of composites. In this study, such properties are extracted from the Fire Dynamic Simulator (FDS).

FDS is a computational fluid dynamics model which solves numerically Navier-Stokes equations, for low-speed, thermally driven flow. Second-order finite-difference approximations are updated in time on a 3D rectilinear grid, for the partial derivatives of conservation equations of mass, momentum and energy. Thermal radiation is computed using a finite volume technique on the same grid as the flow solver.

To simulate a real fire scenario, a considerable amount of details and specifications about the geometry and surrounding space are required. The FDS input file contains information about the numerical grid, ambient environment, building geometry, material properties, combustion kinetics, and desired output quantities. The geometry is characterized by rectangular obstructions that can heat up, burn, conduct heat, etc.; and vents from which air or fuel can be either supplied, or drawn from the flow domain. The dimensions for the FDS geometry can vary from millimeters to tens of meters, and the resolution of the simulation depends on the numerical grid applied. As for the numerical grid, it consists of rectilinear meshes, usually uniform cells. Properties of solid surfaces considered in the simulation such as walls, ceiling, floor and furnishings are provided. Solid surfaces are described by their material properties. Materials are defined by their thermal conductivity, specific heat, density, thickness, and burning behavior.

For each numerical cell at each time step, FDS calculates the gas phase temperature, density, pressure, velocity, and chemical composition. Additionally, solid surface outputs which are associated with the energy balance between the gas and the solid phase are computed such as: temperature (surface and interior), heat flux, mass loss rate and various other quantities. The trajectories of various quantities at a single point are saved in simple, comma-delimited text file. Similarly, fire heat release rates are saved and plotted using a spreadsheet program for further analysis. Solid phase thermocouples are used to record the near surface heat flux of the structural element.

A series of FDS simulations for the following blast-resistant and fire-retardant materials are conducted for the following: polymeric coated cinder blocks (Polyurea, Polyurea + POSS, Polyurea + 6% graphene, Epoxy, Epoxy + 6% graphene, LR, LRFCF, LRHP and Type 4. The objective of this work is to calculate the time evolution function of the heat flux ( $Q$ ) and temperature ( $T$ ), ( $Q(t)$ ,  $T(t)$ ), and to compare the flammability of the different polymeric blast-resistant and fire-retardant materials. Furthermore, the maximum heat flux obtained, from the FDS output files, is applied as thermal loading for the FEA simulations.

The FDS simulations are performed on a grid size of 6.25 cm x 6.25 cm x 6.25 cm grid. The time averages and the grid size are chosen to be compatible with the times scale associated with thermal diffusion through the smallest structural members of

interest. The polymeric coatings are identified as adiabatic surfaces with 3mm thickness, distinguished by assigning the average values of the HRRs per unit area measured from the polymeric coated bricks cone calorimeter testing, and ignition temperature of 350 °C. Assigning the average values of HRRs to the candidate polymer coating, makes the simulations easier to perform because it justifies the use of a single HRR value (rather than a function that describes the dependence of HRR on incident flux), for each candidate material. The time averages and the grid size are chosen to be compatible with the times scale associated with thermal diffusion through the smallest structural members of interest. The same fire scenarios are used in all three cases.

**Table I:** Material Properties for FDS Simulations

Material	Specific Heat (kJ/kg.K)	Density (g/cm <sup>3</sup> )	Conductivity	HRR
Masonry Walls	0.84	14.4	0.48	407
Polymers	2.0	1.0	0.09	HRR*
Gypsum Board	1.2	2.9	0.34	----

Material	Specific Heat (kJ/kg.K)	Density (g/cm <sup>3</sup> )	Conductivity	HRR
*HRRs for polymeric coated cinder blocks are obtained from Table III incident heat flux @ (40 kW/m <sup>2</sup> ) coated bricks				

- Single Room Fire Model

FDS simulations are performed to determine the extent to which various candidate materials contributed to a fire confined to an office space (6m x 3m x 3m high) in a building. The office space has three walls and is open in front. The (533 ± 50 kW) fire is located near the back wall, which is specified by assigning thermo-physical properties consistent with a 3mm coating of the candidate material on concrete. The floor and ceiling are assigned properties typical of gypsum, while the front of the space is left open to the air.

- Concrete Column Model

For the FDS concrete columns simulations, the following geometry dimensions are used: a cross section of (18"x18"=45.72cmx45.72cm), height of (3) m with a 3 mm polymeric coating applied to its surfaces. Solid phase thermocouple devices are placed on the front side of the column (near fire), to measure the temperatures and heat fluxes on the front surface of the coated column during the simulations, at the following heights: (0.1, 0.2, 0.3, 0.4, 0.5, 1.0, 1.5, 2.0, 2.5, 2.6, 2.7, 2.8, and 2.9) m. A demonstration is shown in Figure 1. The simulations are run for 200 s with a time step of 1 s.

- *Masonry Wall Model*

Typical masonry walls of dimensions (3mx3mx0.20m) and (3) mm coating thickness are assembled for FDS numerical simulations. Each masonry wall configuration is simulated for 200 sec at a time step of 1 sec as a part of the single room structural system. As is done for the columns, solid phase thermocouple devices are placed on the front side of the masonry walls (near fire) at heights (0, 0.1, 0.2, 0.3, 0.4, 0.5, 1.0, 1.5, 2.0, 2.5, 2.6, 2.7, 2.8, and 2.9) m (center line of the wall) to record the heat flux and wall temperature during the simulation.

### iii. STRUCTURAL FAILURE (FINITE ELEMENT ANALYSIS)

To evaluate the stresses resulting from subjecting a structure to fire loadings, finite element analysis is performed on two types of structural elements: concrete columns and masonry walls. Coupled thermal/structural analysis is employed using commercially available finite element package ANSYS 11.0. Both types of structures are fixed from the top and the bottom (see Figure 2). The columns and the walls are considered to be coated from the front face only using polymeric coating of 3 mm thick. Fire loading is subjected to the coated surface.

In this study we utilized 8 node brick element type (Solid 70 in the thermal analysis and Solid 45 in the structural analysis) with a constant element size of 0.05 m. The geometry and the mesh are kept constant during the entire analysis. Two sequential loadings (e.g. two load steps) are applied to the structural member: thermal loading followed by structural loading. During the first load step, heat flux is applied to the largest surface area of the structure (front of the structure). Maximum heat fluxes ( $Q_1$ - $Q_{12}$ ), obtained from the solid phase FDS devices is used in this step. For simplicity, a steady state condition for 200 seconds is assumed. Thermal properties for concrete and polymeric coatings are defined as thermally isotropic materials with thermal conductivities of (0.42

W/m<sup>2</sup>.K and 0.14 W/m<sup>2</sup>.K) respectively. Output of the thermal analysis is used as an input for the second load step of structural loading where nodal temperatures from thermal analysis are applied to the front side of the structural member. This loading is applied as a body force in the second step of the subsequent stress analysis. Generic linear elastic and isotropic mechanical and thermal properties of concrete and polymeric coatings are assumed (Table II) during the second load step.

**Table II:** Material Properties for FEA Simulations

Material	Density (g/cm <sup>3</sup> )	Young's Modulus (GPa)	Poisson Ratio	CTE (/°C)
Concrete	2.4	30	0.15	12x10 <sup>-6</sup>
Polyurea	1.2	3.1	0.37	45x10 <sup>-6</sup>
Epoxy	1.2	2.9	0.34	73x10 <sup>-6</sup>
Gypsum	14.4	2.5	0.3	16.2xe <sup>-6</sup>

## **RESULTS AND DISCUSSION**



## **EXPERIMENTAL MEASUREMENTS (CONE CALORIMETER)**

Time dependent HRR (heat flux 30 kW/m<sup>2</sup>) curves obtained from cone calorimeter measurements on polyurea POSS and epoxy graphene plaques (~1.0 cm thick), are displayed in Figure 3. The HRR plateau occurring during the initial stages of the burn is indicative of quasi-steady burning that is characterized by a thin, well-defined pyrolysis zone and constant temperature gradient throughout the sample. This is followed by a dramatic increase in HRR as more and more of the sample thickness became involved in pyrolysis. The burning behavior of the epoxy neat plaques is particularly violent as flaming fragments are observed to shoot out from the top and sides of the burning plaque. The presence of the graphene additive did, however, appear to mitigate this effect. The time dependent HRR plots obtained from cone calorimeter measurements for the polymer-coated cinder blocks are shown in Figure 4. Additionally, peak heat release rates (PHRRs) for the cone calorimeter measurements at (30, 40 and 50) kW/m<sup>2</sup> incident heat fluxes are summarized in Figures 5 and 6.

Although the PHRRs for the polymer plaques are quite high approaching 2000 kW/m<sup>2</sup>, the HRRs from the polymer coated cylinder blocks are much more modest as indicated in Figures 5 and 6. Furthermore, as revealed by Figure 6, the presence of the cinder blocks effectively eliminates the strong dependency of HRR on incident heat flux that is observed for the corresponding polymer plaques.

The data listed in Table III indicate that while the presence of the additives (POSS, phosphate, graphene) tends to reduce the HRRs of the polymer plaques, they do not seem to provide much benefit when these materials are used as coatings on cinder blocks. Indeed, the presence of graphene appears to increase the HRR of the epoxy coating significantly.

The results obtained from the cone calorimeter tests indicate that the fire performance of the commercial LR fire retardant is far better than any of the other coatings examined in this study. During the tests on the LR coated blocks, it is observed that the flames are confined to a small fraction of the surface.

**Table III:** PHHRs for Candidate Material

<b>Material</b>	<b>Incident Flux (30 kW/m<sup>2</sup>)</b>	<b>Incident Flux (40 kW/m<sup>2</sup>)</b>	<b>Incident Flux (50 kW/m<sup>2</sup>)</b>
<b>Polymeric Plaques</b>			
Polyurea	1450	1875	2201
Polyurea Phosphate	n.a.	1720	1327
Polyurea POSS	856	1299	1156

Material	Incident Flux	Incident Flux	Incident Flux
	(30 kW/m <sup>2</sup> )	(40 kW/m <sup>2</sup> )	(50 kW/m <sup>2</sup> )
Epoxy	1544	1966	2263
Epoxy Graphene	1738	1553	1887
Polymeric Coated Cinder Blocks			
Polyurea	213	260	216
Polyurea POSS	233	229	293
Polyurea Graphene	305	261	221
Epoxy	391	422	n.a.
Epoxy Graphene	602	552	552
LR	---	38	39
LRHP	---	127	152
LRFCF	---	84	108
Type 4	---	128	147

The polyurea appears to perform better than the epoxy, which has higher PHRRs, drips, and spalls, sending burning fragments of the epoxy flying off the blocks during the experiments. The presence of the graphene mitigates the dripping and spalling observed in the pure epoxy coated bricks and generally delays ignition times (Figure 3). Unfortunately, the graphene also appears to increase PHRR at low thermal flux. The longer ignition times and higher PHRRs may be due to an increase in thermal conductivity imparted by the graphene.

## **NUMERICAL SIMULATIONS (FIRE DYNAMIC SIMULATOR)**

### **i. SINGLE ROOM FIRE MODEL**

Snapshots of the maximum heat release rate per unit volume (HRRPUV) from the simulations generated by FDS are shown for the various coatings in Figure 7, the snapshots are taken around 120 seconds.

The blast-resistant and the fire-retardant coatings are distinguished by assigning the average values of the HRRs (per unit area) measured in the cone calorimeter tests. This justification will simplify the simulation input of a single HRR value (rather than a function that describes the dependence of HRR on incident flux) for each simulated candidate material. The coatings are programmed to ignite when the surface temperature exceeded 350 °C. The maximum HRR of the room fire simulated for each coating and the control (bare concrete) are listed in Table IV.

These data indicate that the LR and Type 4 fire retardant coatings are very effective in reducing the HRR from the polymer coated walls. The effect of the addition of POSS and graphene to the polyurea and epoxy coatings is either minimal or, in the case of the epoxy, counterproductive.

**Table IV:** Concrete Coated Blocks Maximum HRR of Simulated Fires

Coating Material	Max HRR (kW/m <sup>2</sup> )
No Coating	593
Polyurea	850
Polyurea POSS	827
Polyurea Graphene	829
Epoxy	1120
Epoxy Graphene	1520
LR	605
LRFCF	586
LRHP	621
Type4	608

Fire smoke is a mixture of small fragments of fiber and ultra fine carbon particles (soot). The amount of smoke produced when a composite material burns is a concern because smoke obscures visibility thereby making it difficult for occupants to escape from the fire. Thus, if

all other factors are equal, materials that produce a lot of smoke when they are burned are less safe than materials that produce less smoke. Figure 8 shows smoke snapshots at 100 sec for the room FDS model. The black color for polyurea POSS indicates smoke generation associated with fire and reduction in visibility compared to the fire retardant coatings.

## ii. CONCRETE COLUMN MODEL

Figure 9 demonstrates the heat release rate per unit volume (HRRPUV) snapshots for the different simulated coated columns. The snapshots presented are taken at 100 seconds; they are comparable in terms of flame characterization. It appears that the flame is the least for the polyurea POSS and the greatest for the epoxy graphene coated columns. Figure 10 shows the maximum values of the heat flux plots as a function of time at height (0.50)m from the floor. Table V summarize the maximum heat flux captured by the solid phase devices described above. Not surprisingly, the results in Table V confirm that the polymeric coatings have increased the heat transfer per unit area compared to the uncoated and gypsum covered concrete columns which do not contribute to the HRR. We note further that the gypsum covering is very effective in insulating the concrete columns from the heat generated by the existing fire. Table V results are used as thermal loading for the FEA concrete columns simulations.

**Table V:** Maximum Q(t) Coated Concrete Columns Simulations (kW/m<sup>2</sup>)

Device Height (m)	Concrete	Polyurea	Polyurea POSS	Epoxy	Epoxy Graphene	Gypsum
0	0.485	0.436	0.425	0.40	0.386	1.16
0.1	2.173	1.972	1.963	1.86	1.761	3.07
0.2	35.234	28.727	29.017	29.85	25.687	11.93
0.3	38.201	36.123	36.263	33.61	36.912	13.38
0.4	34.775	39.752	39.226	31.43	39.515	12.68
0.5	28.578	39.710	37.062	26.71	37.611	11.37
1	4.501	8.754	6.807	5.85	5.412	2.19
1.5	2.066	3.054	2.737	2.74	0.756	0.71
2	1.304	2.106	1.987	1.66	0.391	0.55



Device Height (m)	Concrete	Polyurea	Polyurea POSS	Epoxy	Epoxy Graphene	Gypsum
2.5	1.083	1.632	1.536	1.35	0.339	0.64
2.6	0.956	1.496	1.381	1.31	0.325	0.59
2.7	0.841	1.355	1.240	1.25	0.316	0.53
2.8	0.754	1.219	1.122	1.20	0.313	0.47
2.9	0.738	1.108	1.013	1.18	0.309	0.42

### iii. MASONRY WALL MODEL

Figure 11 demonstrates the heat flux  $Q(t)$  evolution for the coated masonry walls. Figure 12 indicates that the addition of POSS to polyurea tends to lower the monitored surface temperature. Table VI below summarizes the maximum heat flux captured by the solid phase devices at mentioned heights. However, LR has shown the minimum released heat fluxes and surface temperatures. Results shown in Table VI are employed as thermal loading for the FEA masonry walls.

**Table VI:** Maximum  $Q(T)$  Coated Masonry Walls Simulation ( $\text{kW/m}^2$ )

Device Height (m)	Polyurea	Polyurea POSS	Polyurea Graphene	Epoxy	Epoxy Graphene	LR	LR HP	LR FC F	Type 4
0	11.93	11.1	13.0	13.4	13.0	9.8	10.5	9.7	9.8
0.1	14.70	13.4	---	---	---	13.0	12.8	13.0	12.1
0.2	31.97	24.0	---	---	---	26.7	22.7	27.4	22.5
0.3	40.79	24.7	---	---	---	29.7	30.1	30.6	29.8
0.4	46.34	37.5	---	---	---	32.8	36.8	34.0	33.6
0.5	48.59	45.1	46.3	51.7	56.1	33.1	39.4	34.3	34.5
1	51.15	47.3	51.1	59.9	61.3	27.0	37.6	27.5	30.5
1.5	46.52	49.5	51.8	59.9	66.0	17.2	23.8	17.4	15.8
2	28.50	45.0	50.7	59.9	65.6	11.1	19.7	10.0	13.5
2.5	18.93	22.9	52.3	62.5	63.4	8.4	16.6	8.1	15.2
2.6	18.29	17.7	---	---	---	8.3	17.2	8.0	15.8
2.7	17.33	17.2	---	---	---	8.2	17.6	7.9	17.4
2.8	16.80	16.2	---	---	---	8.1	17.7	7.8	17.7
2.9	15.94	15.8	---	---	---	8.2	18.4	7.4	17.9

## FINITE ELEMENT SIMULATIONS

### i. CONCRETE COLUMN MODEL

Spatial and temporal variation in temperature distribution results in thermally induced stresses/strains and reduced bearing capacity. A typical nodal temperature distribution for a concrete column is demonstrated in Figure 13.

A time dependent thermal nodal analysis is adapted to calculate the temperature nodal distribution and to reveal the thermal response of the concrete columns that can potentially result in structural failure (as described in section: STRUCTURAL FAILURE (FINITE ELEMENT ANALYSIS)).

The von Mises stresses/strains are shown Figures 14 and 15. The polyurea based nanocomposites performed better than the epoxy based in term of maximum stresses/strains.

## ii. MASONRY WALL MODEL

The fire effect of polymer reinforced composites coated masonry walls is studied using ANSYS coupled thermal/structural analysis (as described in section: STRUCTURAL FAILURE (FINITE ELEMENT ANALYSIS)). The maximum/minimum stresses/strains are obtained for the coated masonry walls with the blast-resistant and fire-retardant coatings. The masonry walls are exposed to the heat fluxes per unit area collected from solid phase devices installed on the front side of the masonry wall from the FDS simulations. A typical nodal temperature distribution is shown in Figure 17.

The total mechanical Von Mises stress/strains contour plots are shown in Figures 17 and 18. The results confirm that the polyurea POSS coated masonry walls performed the best in terms of mechanical stress and strain performance compared to the other polymeric blast-resistant coatings.

## **CONCLUSIONS**

The blast-resistant material coatings have similar behavior in terms of maximum heat flux and stress/strains. The addition of POSS or graphene has been shown to reduce the HRR of polyurea. On the other hand, addition of graphene platelets to epoxy coatings has the opposite effect; increasing the HRR, maximum heat flux and maximum surface temperatures. The simulations indicate that fire-retardant coatings, such as LRFCF and HP, are effective in reducing the peak HRR of an existing fire. LR performed the best in terms of maximum HRR and smoke density and visibility.

Whereas the main objective of this paper is to evaluate fire performance of materials developed originally with an intention of improving blast performance of structures an optimized blast/fire system is still under investigation.

VITA

The University of Mississippi University, Mississippi

Bachelor of Science, Civil Engineering May 2011

